Trafficking of the glutamate transporter is impaired in LRRK2-related Parkinson's disease

Ludovica Iovino [1], Veronica Giusti [1], Francesca Pischedda [2], Elena Giusto [3], Nicoletta Plotegher [1], Antonella Marte [4], Ilaria Battisti [5], Angela Di Iacovo [6], Algerta Marku [7], Giovanni Piccoli [2], Rina Bandopadhyay [8], Carla Perego [7], Tiziana Bonifacino [9], Giambattista Bonanno [9,10], Cristina Roseti [6], Elena Bossi [6], Giorgio Arrigoni [5], Luigi Bubacco [1], Elisa Greggio [1], Sabine Hilfiker [11], Laura Civiero [1,3]*

[1] Department of Biology, University of Padova, Italy

[2] University of Trento, Department of Cellular, Computational and Integrative Biology – CIBIO, Trento, Italy

[3] IRCCS San Camillo Hospital, Venice, Italy

[4] University of Genova, Department of Experimental Medicine, Genova, Italy;

[5]Department of Biomedical Sciences, University of Padova, Padua, Italy

[6] Department of Biotechnology and Life Sciences, Center for Research in Neuroscience, University of Insubria, Varese

[7]University of Milano, Department of Pharmacological and Biomolecular Sciences, Milano, Italy;

[8]Reta Lila Weston Institute of Neurological Studies, UCL Queen Square Institute of Neurology, London, WC1N 1PJ, United Kingdom;

[9]University of Genova, Department of Pharmacy-DIFAR, Genoa, Italy

10 IRCCS Ospedale Policlinico San Martino, Genoa, Italy

[11]Rutgers New Jersey Medical School, Department of Anesthesiology and Department of Physiology, Pharmacology and Neuroscience, Newark, New Jersey, United States of America;

*Correspondence:

Laura Civiero, PhD

laura.civiero@unipd.it

Phone number: +39 0498276233

Running title: G2019S LRRK2 alters Glt-1 trafficking

Abstract

The Excitatory Amino Acid Transporter 2 (EAAT2) accounts for 80 % of brain glutamate clearance and is mainly expressed in astrocytic perisynaptic processes. EAAT2 function is finely regulated by endocytic events, recycling to the plasma membrane and degradation. Noteworthy, deficits in EAAT2 have been associated with neuronal excitotoxicity and neurodegeneration. In this study, we show that EAAT2 trafficking is impaired by the leucine-rich repeat kinase 2 (LRRK2) pathogenic variant G2019S, a common cause of late-onset familial Parkinson's disease (PD). In LRRK2 G2019S human brains and experimental animal models, EAAT2 protein levels are significantly decreased, which is associated with elevated gliosis. The decreased expression of the transporter correlates with its reduced functionality in mouse LRRK2 G2019S purified astrocytic terminals and in *Xenopus laevis* oocytes expressing human LRRK2 G2019S. In Lrrk2 G2019S knockin mouse brain, the correct surface localization of the endogenous transporter is impaired, resulting in its interaction with a plethora of endo-vesicular proteins. Mechanistically, we report that pathogenic LRRK2 kinase activity delays the recycling of the transporter to the plasma membrane, causing its intracellular relocalization and degradation. Taken together, our results demonstrate that pathogenic LRRK2 interferes with the physiology of EAAT2, pointing to extracellular glutamate overload as a possible contributor to neurodegeneration in PD.

Keywords

LRRK2, Glt-1, EAAT2, glia, astrocytes, Parkinson's disease

Introduction

The concentration of extracellular glutamate in the central nervous system is finely tuned by specific excitatory amino acid transporters (EAATs) [1,2], which remove the neurotransmitter from the extracellular synaptic milieu and prevent the dramatic consequences of glutamate accumulation [3-9]. Impaired glutamate uptake entails neuropathological consequences such as alteration of synaptic neurotransmission, neuronal excitotoxicity as well as astro- and microgliosis and neurodegeneration [10,11]. Among EAATs, EAAT2 (corresponding to glutamate transporter type 1, Glt-1 in rodents) is the predominant glutamate transporter in the adult mammalian brain and accounts for the removal of most of the extracellular glutamate [12,13]. Approximately 80 to 90 % of EAAT2 is localized on astrocytes, and 5 to 10 % on the axonal terminal of neurons [4-9].

Regulation of EAAT2 function occurs by protein expression and protein distribution. Indeed, both lateral diffusion and endocytic trafficking ensure a dynamic turnover of the receptor at the synaptic terminals that reflects the shuffling activity of neighboring cells [3,14-16]. EAAT2 is constitutively internalized into recycling endosomes via a clathrin-dependent pathway, which relies on the reversible ubiquitination of specific lysine residues located in the cytoplasmic C-terminus [17]. The ubiquitin ligase Nedd4-2 has been identified as a mediator of EAAT2 endocytosis [18]. The activation of protein kinase C (PKC) promotes the phosphorylation of Nedd4-2, its association with EAAT2 and the subsequent ubiquitination of the transporter [19]. Importantly, a ubiquitination/de-ubiquitination cycle enables a reversal translocation of EAAT2 from the recycling endosomes back to the plasma membrane. Therefore, a strict regulation of this bidirectional trafficking is crucial to guarantee an appropriate exposure of EAAT2 at the cell surface [17,20]. Interference with EAAT2 trafficking has been often associated with the re-routing of the transporter to the cellular degradative systems [21-24].

Parkinson's disease (PD) is a progressive neurodegenerative disorder clinically characterized by severe motor disability and cognitive impairment [25]. The pathological hallmarks of PD include the selective loss of dopaminergic neurons in the *Substantia Nigra pars compacta* (*SNpc*) that project to the dorsal striatum, the presence of Lewy Bodies in neuronal and glial cells, as well as signs of extended neuroinflammation [26-28]. Despite decades of research, the mechanisms underlying the selective degeneration of dopaminergic neurons in PD remain unclear [29]. Recent hypotheses support the idea that chronic, subtle dysfunctions, both at cellular and non-cellular levels, proceed years before the clinical symptoms and the dopaminergic death [30]. Perturbation of

glutamate homeostasis is one of the earliest events in the pathophysiology of PD and contributes to the exacerbation of later clinical impairments [11,31-34]. In addition, deficits in glutamate transporters have been consistently reported upon acute neurotoxin injection in rodents [18,35,36] as well as in genetic models of PD [33,37,38], and selective ablation of nigral astrocytic Glt-1 expression induces a parkinsonian-like phenotype in mice [39].

Monogenic mutations with Mendelian transmission have been identified in about 10 % of PD cases [40], and mutations in the leucine-rich repeat kinase 2 (LRRK2) account for up to 40 % of familial PD forms. Specifically, the most common LRRK2 p.G2019S mutation leads to the expression of a hyperactive form of the LRRK2 kinase and appears in approximately 1 % of apparently sporadic PD cases, with much higher prevalence in specific ethnic groups [41]. Although LRRK2 G2019S animal models do not show clear signs of neurodegeneration, aberrant cortico-striatal glutamatergic neurotransmission has been observed, thus comprising a valuable model system to study the early stages of the disease [42-44].

Here, we report that the PD-linked LRRK2 G2019S mutation decreases the functionality of EAAT2 in astrocytes by impairing its recycling to the plasma membrane. Overall, our results point to glutamatergic dysregulation as a key pathological event in PD.

Materials and methods

Human samples

Post-mortem human basal ganglia lysates in RIPA buffer (20mM Tris-HCl pH 7.5, 150mM NaCl, 1mM EDTA, 2.5mM sodium pyrophosphate, 1mM β-glycerophosphate, 1mM sodium orthovanadate) containing protease and phosphatase inhibitors (Roche) derived from four LRRK2 G2019S-linked patients and 10 age-matched controls were obtained from Queen Square Brain Bank (London, UK). *Post-mortem* human brains were collected under human tissue authority license n° 12198. Limited sample demographics are listed in *Table 1*.

Animals

C57Bl/6J Lrrk2 wild-type (WT) and Lrrk2 G2019S knock-in mice were used. Lrrk2 G2019S knock-in mice were obtained from Prof. Michele Morari and Novartis Institutes for BioMedical Research, Novartis Pharma AG (Basel, Switzerland) [45]. Housing and handling of mice were done in compliance with national guidelines. All procedures performed in mice were approved by the Ethical Committee of the University of Padova and the Italian Ministry of Health (license 1041/2016, 200/2019 and 105/2019). All procedures performed in *Xenopus laevis* were approved and experiments carried out according to Ethical Committee of the University of Insubria (license no. 02_15) and the Italian Ministry of Health (1011/2015).

Immunoblotting

Human basal ganglia samples as well as dissected striata derived from Lrrk2 WT and Lrrk2 G2019S knock-in mice were lysed in RIPA buffer containing 1 % protease inhibitor cocktail (Sigma-Aldrich). Protein concentration was measured using the Pierce® BCA Protein Assay Kit following manufacturer's instructions (Thermo Scientific). 25 µg protein samples were resolved by electrophoresis on pre-cast 4–20 % tris-glycine polyacrylamide gels (Biorad) and transferred to polyvinylidenedifluoride membranes using a semi-dry Biorad transfer machine (Trans-Blot® Turbo TM Transfer System) with the 1X Transfer Buffer (BioRad) at 25 V for 20 min. Membranes were incubated in Tris-buffered saline plus 0.1 % Tween (TBS-T) plus 5 % skimmed milk for 1 h at room temperature (RT), and then incubated overnight with primary antibodies diluted in TBS-T plus 5 % skimmed milk. The following primary antibodies were used: guinea pig anti-glutamate transporter (Glt-1/EAAT2; AB1783, EMD Millipore, 1:500), mouse anti-GAPDH (CSB-MA000195, Cusabio, 1:3000), mouse anti-β-actin (A1978, Sigma-Aldrich, 1:10000), mouse anti-HSP70 (H5147; Sigma Aldrich, 1:5000), rabbit anti-glial fibrillary acidic protein (GFAP; Z0334, Dako 1:20000/1:100000), rabbit anti-glutamine synthetase (GS; GTX109121, GENETEX, 1:1000)

and rabbit anti-Tyrosine Hydroxylase (TH; AB152, EMD Millipore, 1:1000). Membranes were subsequently rinsed and incubated for 1 h at RT with the appropriate HorseRadish-Peroxidase (HRP)-conjugated secondary antibodies (Invitrogen). The visualization of the signal was conducted using Immobilon® Forte Western HRP Substrate (Millipore) and the VWR® Imager Chemi Premium. Images were acquired and processed with ImageJ software to quantify total intensity of each single band.

Human basal ganglia immunofluorescence and immunohistochemistry analysis

Paraffin embedded sections (8 µm) from human brain areas were cut using a microtome (Thermo Scientific). To remove paraffin wax, 8 µm-slices were washed in xylene and rehydrated in 100 % ethanol. Slices were treated for 15 min with a quenching solution containing 50 mM NH_4Cl in phosphate buffer saline (PBS) for immunofluorescence analysis, or 100 % methanol and 3 % H_2O_2 for immunohistochemistry studies. Slices were then washed in TBS-T and incubated at 90° C for 15 min with a citrate buffer (10 mM Sodium Citrate and 0.1M citric acid dissolved in distilled water; pH 7.0) to perform epitope retrieval. Subsequently, slices were saturated for 1 h at RT in a blocking solution containing 1 % bovine serum albumin (BSA), 15 % goat serum, 0.25 % gelatin, 0.20 % glycine and 0.5 % Triton. Slices were then incubated overnight at 4 °C with the following primary antibodies diluted in blocking solution: guinea pig anti-EAAT2 (1:200) and/or rabbit anti-GFAP (1:400). The following day, slices were washed in TBS-T and incubated for 1 h at RT with a mixture of the following secondary antibodies diluted 1:200 in blocking solution: anti-guinea pig Alexa Fluor 488 (Life Technologies) and anti-rabbit Alexa Fluor 568 (Life Technologies) fluorophores. Upon washes in TBS-T, slices were incubated for 5 min with Hoechst (1:10000; Invitrogen) to visualize the nuclei and mounted with Mowiol (Calbiochem).

For immunohistochemistry analysis, sections processed with rabbit anti-GFAP were incubated for 1 h at RT using secondary HRP-conjugated anti-rabbit antibody (1:200). Slices were then washed and developed for 2-3 min using 3,3′-diaminobenzidine (DAB) staining kit (Abcam; #ab64238;). Nuclei were counterstained using Haematoxylin (MHS32-Sigma) for 5 min. Finally, sections were dehydrated in graded ethanol (70%, 90% and 100%), transferred in xylene and mounted using a Eukitt Mounting resin (Kirsker Biotech).

Plasmids

The pCMV-hEAAT2 plasmid encoding the human excitatory amino acid transporter type 2 (EAAT2) was a gift from Susan Amara (Addgene plasmid # 32814; http://n2t.net/addgene:32814; RRID:Addgene_32814). The cDNA was subcloned into pcDNA3 between KpnI and XbaI

restriction sites and under the T7 promoter for expression in *Xenopus laevis* oocytes. The pDESTN-SF-TAP LRRK2 plasmids encoding the human WT and G2019S variant were described in [46]. The pCMV6-mGLT-1 (Myc-DDK-tagged) plasmid encoding the mouse glial high affinity glutamate transporter member 2 (Slc1a2), transcript variant 1, was purchased from OriGene Technologies Inc (Cat. MR226166). For the pEGFP-rat Glt1 plasmid, the 99-1820 bp fragment of the Rat Glt-1 plasmid (GenBankTM accession number X67857.1) was subcloned between the EcoRI and Xba restriction sites of pEGFP vector (Clontech). GFP-Rab4, GFP-Rab11 and GFP-Lamp1 plasmids were generated as previously described [47,48].

Electrophysiological recordings in *Xenopus laevis* oocytes

pcDNA3_hEAAT2 and pDESTN-SF-TAP-LRRK2 WT and G2019S plasmid vectors were linearized by HindIII and SmaI, respectively. Corresponding cRNAs were transcribed *in vitro* and capped using T7 RNA polymerase. Oocytes were obtained by laparotomy from adult female Xenopus laevis (Envigo). Frogs were anesthetized by immersion in MS222 1 g/L solution in tap water adjusted at final pH 7.5 with bicarbonate. After the treatment with an antiseptic agent (povidone-iodine 0.5 %), the frog abdomen was incised, and the portions of the ovary removed. Oocytes were treated with 1 mg/mL collagenase IA (Sigma Collagenase from Clostridium histolyticum) in calcium-free ND96 (96 mM NaCl, 2 mM KCl, 1 mM $MgCl_2$, 5 mM 4-(2-hydroxyethyl)-1-piperazineethanesulfonic acid (HEPES); pH 7.6) for at least 1 h at 18 °C. Healthy and fully grown oocytes were selected and manually separated in NDE solution (ND96 plus 2.5 mM pyruvate, 0.05 mg/mL gentamicin sulphate and 1.8 mM $CaCl_2$). After 24 h, healthy looking stage V and VI oocytes were collected and co-injection of cRNA EAAT2 (25 ng) + cRNA LRRK2 WT (25 ng) or cRNA EAAT2 (25 ng) + LRRK2 G2019S (25 ng) was carried out using a manual microinjection system (Drummond Scientific Company). Oocytes were subsequently incubated at 18 °C for 2-3 days in NDE solution [49]. Transport currents (I) were recorded from voltage-clamped oocytes using two microelectrodes filled with 3 M KCl (Oocyte Clamp OC-725C, Warner Instruments). Bath electrodes were connected to the experimental oocyte chamber via agar bridges (3 % agar in 3 M KCl). The external control solution had the following composition: 98 mM NaCl, 1 mM $MgCl_2$, 1.8 mM $CaCl_2$, 5 mM HEPES, adjusted to pH 7.6 with NaOH. Signals were filtered at 0.1 kHz and sampled at 200 Hz or 0.5 kHz and at 1 kHz. Transport-associated currents were calculated by subtracting the traces in the absence of substrate from those in its presence. To measure the apparent affinity for glutamate (the concentration of glutamate that yields one-half of the maximal transport current), oocytes were exposed to different neurotransmitter concentrations

(10 µM, 25 µM, 100 µM, 500 µM, 1 mM). Clampex and Clampfit 10.7 (Molecular Devices) were used to run the experiments, acquire and analyse the data.

Immunodetection in *Xenopus laevis* oocytes

Injected oocytes were fixed in ice-cold 4 % paraformaldehyde (PFA) in PBS pH 7.5, for 15 min at 4 °C. Oocytes were subsequently washed using ND96 in mild agitation (5 min at RT, three times), included in Polyfreeze tissue freezing medium (Polysciences, Eppelheim) and frozen in liquid nitrogen. Oocyte cryosections (10 µm thickness) were obtained with a cryostat (Leica Biosystems) and preserved at -20 °C. Before use, oocyte slices were washed in PBS for 10 min at RT and incubated in blocking solution (2% BSA (w/v), 0.1 % Tween in PBS) for 45 min. Slices were then incubated overnight at 4 °C with the primary antibody guinea pig anti-EAAT2 (1:200) diluted in blocking solution. The following day, oocyte sections were washed in PBS and incubated with the secondary antibody anti-guinea pig Alexa Fluor 488 fluorophore diluted 1:200 in blocking buffer for 1 h. Sections were washed and mounted using Mowiol. Images were acquired at 8-bit intensity resolution over 1024x1024 pixel on a Leica SP5 confocal microscope using a HC PL FLUOTAR 40x/0.70 oil objective. Using ImageJ, EAAT2 the integrated fluorescence density (IntDen, area x mean fluorescence) was measured by defining a ROI (8×10^{-3} mm^2 area). All quantifications were applied at the animal pole of the oocytes.

Free-floating mouse brain slice immunofluorescence

Mice were anesthetized with xylazine (Rompun®) and ketamine (Zoletil®) and transcardially perfused with physiological solution (0.9 % NaCl in PBS) followed by ice-cold 4% PFA dissolved in PBS at pH 7.4. Brains were post-fixed at 4 °C for 18 h in 4 % PFA and then moved in two different solutions of sucrose (20 % and 30 % sucrose in PBS) for 18 h each. Coronal striatal sections (30 µm thickness) were sliced using a vibratome (Campden Instruments Ltd.). Slices were stored at 4 °C in a solution containing 18 % sucrose, 0.01 % NaN_3 dissolved in PBS. Before staining, slices were rinsed in PBS and treated with 50 mM NH_4Cl dissolved in PBS for 15 min at RT to quench intrinsic autofluorescence. Sections were then washed in PBS followed by permeabilization and saturation for 1 h at RT in a blocking solution containing 2 % BSA, 15 % goat serum, 0.25 % gelatin, 0.2 % glycine and 0.5 % Triton. Slices were then incubated overnight with primary antibodies diluted in blocking solution. The following primary antibodies were used: guinea pig anti-Glt-1 (1:200) and rabbit anti-GFAP (1:400). The following day, slices were washed and incubated for 1 h at RT with the appropriate secondary antibodies diluted in blocking solution: anti-guinea pig Alexa Fluor 488 and anti-rabbit Alexa Fluor 568 fluorophores. Upon incubation,

slices were washed with PBS and nuclei were counterstained with Hoechst 1:10000 and mounted on a glass microscope slide (ThermoFisher) using Mowiol.
Images were acquired at 8-bit intensity resolution over 1024x1024 pixel on a Leica SP5 confocal microscope using a HC PL FLUOTAR 40x/0.70 oil objective. Using ImageJ, the integrated density (IntDen, area x mean fluorescence) of GFAP signal upon setting scale and threshold were measured. The number of $GFAP^+$ cells was manually counted using the same software.

Gliosome purification

Glial perisynaptic processes (gliosomes, [50-52]) derived from 4 month old Lrrk2 WT and Lrrk2 G2019S mouse striata were used. Gliosomes were prepared as previously described [53]. Briefly, striata were homogenized in 0.32 M sucrose, buffered at pH 7.4 with Tris-HCl, using a glass-teflon tissue grinder (clearance 0.25 mm – Potter-Elvehjem VWR International). The homogenate was centrifuged (5 min, 1000g) to remove nuclei and debris, and the supernatant was gently layered on a discontinuous Percoll gradient (2 %, 6 %, 10 %, and 20 % v/v in Tris-buffered 0.32 M sucrose; Sigma-Aldrich). After centrifugation at 33500g for 5 min, the layer between 2 % and 6 % Percoll (gliosomal fraction) was collected and washed with a physiological medium having the following composition: 140 mM NaCl, 3 mM KCl, 1.2 mM $MgSO_4$, 1.2 mM NaH_2PO_4, 5 mM $NaHCO_3$, 1.2 mM $CaCl_2$, 10 mM HEPES, 10 mM glucose, pH 7.4, and centrifuged at 20000g for 15 min. The pellet was resuspended in physiological medium. All the above procedures were conducted at 4 °C. Protein concentration was measured using the Pierce® BCA Protein Assay Kit following manufacturer's instructions.

Glutamate uptake assay in gliosomes

Glutamate uptake was measured in striatal gliosomes derived from Lrrk2 WT and Lrrk2 G2019S mice as previously described [54]. Briefly, aliquots of the gliosomal suspensions (500 µL, corresponding to 10-15 µg protein per sample) were incubated for 10 min at 37 °C in the presence of 10 µM 2-amino-5,6,7,8-tetrahydro-4-(4-methoxyphenyl)-7-(naphthalen-1-yl)-5-oxo-4H-chromene-3-carbonitrile (UCPH-101; Abcam 120309, UK), a specific excitatory amino acid transporter 1 (EAAT1/Glast) inhibitor [55]. Then, 20 µL of a solution of [^{3}H]D-Aspartate ([^{3}H]D-Asp; specific activity: 16.5 Ci/mmol; Perkin Elmer) and non-radioactive D-Asp (Sigma Aldrich) was added to each sample to obtain the final concentrations of 0.03, 0.1, 1, 3, 30 and 100 µM. Incubation was continued for further 2 min. Gliosomal samples were exposed to the above [3H]D-Asp concentrations for 2 min at 0–4°C, in the presence of 50 µM of the broad spectrum glutamate transporter blocker DL-threo-beta-benzyloxyaspartate (DL-TBOA; Tocris Bioscience; [56]), to

determine the non-specific binding to gliosome membranes. After the 2-min exposure to [^{3}H]D-Asp, uptake was blocked by rapid vacuum filtration (GF-B filters, Millipore) and filters were washed three times with 5 mL of physiological medium to remove the excess of radioactivity. Radioactivity was determined by liquid scintillation counting. The specific uptake was calculated by subtracting non-specific binding from the total filter radioactivity.

Liquid-chromatography mass spectrometry (LC-MS) analysis

Endogenous Glt-1 was immunoprecipitated from homogenized of WT and *Lrrk2* G2019S mouse striata using 5 µg of a rabbit anti-Glt-1 antibody (Abcam; ab205248) in RIPA buffer (1.5 mg of total protein each). Magnetic beads (Protein A/G Magnetic Beads, BioTool) (50 µL) were used to pre-clear and precipitate the transporter. Beads were then washed three times using 1 mL of RIPA buffer and proteins loaded on pre-cast 4–20 % tris-glycine polyacrylamide gels (Biorad). Gel bands were excised, cut into small pieces and destained with a solution of 60 % NH_4HCO_3 200 mM/40 % acetonitrile (ACN) at 37 °C. Disulfide bridges were reduced with 2 mM Tris (2-carboxyethyl)phosphine hydrochloride (TCEP) in 50 mM NH_4HCO_3 at 56 °C for 1 h, and cysteine residues were alkylated with 4 mM methyl methanethiosulfonate (MMTS) with 50 mM NH_4HCO_3 in the dark at RT for 45 min. Gel samples were washed twice with 50 mM NH_4HCO_3 and ACN alternatively and vacuum-dried. Samples were incubated with 12.5 ng/µL trypsin (Sequencing Grade Modified Trypsin, Promega) in 50 mM $(NH_4)_2HCO_3$ and protein digestion was carried out overnight at 37 °C. Peptides were extracted with three changes of 50 % ACN/ 0.1 % formic acid (FA). Samples were vacuum-dried and stored at −20 °C. Samples were analyzed using a LTQ Orbitrap XL mass spectrometer (Thermo Fisher Scientific) coupled to a HPLC Ultimate 3000 (Dionex - Thermo Fisher Scientific) through a nanospray source (NSI), as described in Battisti et al. 2021 [57]. Samples were resuspended in 30 µL of 3 % ACN/0.1 % FA and each sample was acquired twice. Raw data files were analyzed with MaxQuant [58] software (v. 1.5.1.2) interfaced with Andromeda search engine. Protein search was performed against the mouse section of the UniProt database (Mus musculus, version 2020-09-30, 55494 entries). Enzyme specificity was set to trypsin with up to one missed cleavage allowed, while methylthio-cysteine and oxidized methionine were set as fixed and variable modifications, respectively. A minimum of two peptides was required for protein identification, and a false discovery rate (FDR) $\leq$ 0.01, both at the peptide and protein level, was used to filter the results. To estimate the relative protein abundance accross samples, the intensity values calculated by the software were used. The datasets were compared to highlight significant differences in the protein abundances: common and unique Glt-1 binders between the Lrrk2 WT and G2019S genetic environments were identified performing a Z-test on the log-

transformed values of the IP/CTRL ratios and taking into account only proteins with $p < 0.05$ and Fold Changes (FC) ≥ 3.5. Gene Ontology (GO) terms were employed to identify discrete functional enrichments in order to extract information about novel networks of interactors in relationship to the different subcellular localization of the transporter. G:profiler (https://biit.cs.ut.ee/gprofiler/gost) was used for enrichment analysis. Glt-1-related protein networks in Lrrk2 G2019S pathogenic background were ranked based on the fold-change affinity over the control ($\geq$3.5).

Primary striatal astrocytes

Mouse primary striatal astrocytes were obtained from postnatal animals between day 1 and day 3 as described in [59]. Brains were removed from their skull and placed in a dish containing cold Dulbecco's Phosphate Buffered Saline (DPBS, Biowest). Olfactory bulbs and cortices were removed under an optic microscope and striata were transferred to a separate dish containing cold DPBS. After the dissection, Basal Medium Eagle (BME, Biowest), supplemented with 10 % Fetal Bovine Serum (FBS, Corning), 100 U/mL Penicillin + 100 µg/mL Streptomycin (Pen-Strep; Life Technologies), was added to the tissues. Striata were then sifted through a 70-µm cell strainer (Sarstedt) using a syringe plunger. The cell suspension was centrifuged (300 x g, 15 min) and the pellet was washed twice with 25 mL of supplemented medium. Cells were seeded at a density of $5x10^6$ cells/10 mL in cell culture T75 flasks. The culture medium was changed after seven days and again after an additional 3-4 days. When cell confluency reached about 80 %, microglia were detached by shaking the flask (800 rpm) for 2 h at RT. After shaking, the medium containing microglia was replaced with fresh medium. Cells were maintained in BME supplemented with 10 % FBS and Pen-Strep at 37 °C in a controlled 5 % CO_2 atmosphere. After 14 days, astrocytes were used for the experiments.

Cell transfection

Astrocytes were seeded at a density of $1x10^5$ cells on 12 mm glass coverslips (VWR) coated with poly-L-lysine. Once 80 % of confluency was reached, cells were transfected using Lipofectamine 2000 (Thermo Scientific) (1:3 DNA/Lipofectamine ratio). For single transfection experiments, 1 µg Myc-DDK-tagged-GLT-1 plasmid was used per each well; for double transfection experiments, 0.5 µg Myc-DDK-tagged-GLT-1 was combined with either 0.5 µg GFP-Rab4, GFP-Rab11 or GFP-Lamp1 plasmids. For TIRFM experiments, astrocytes were seeded at a density of $4x10^5$ cells in 24 mm glass coverslips (VWR) coated with poly-L-lysine. Once at 80 % confluence, cells were transfected with 2.5 µg GFP-GLT-1 plasmid using Lipofectamine 3000

(Invitrogen) (1:2 DNA/Lipofectamine ratio). All experiments were carried out 48 hours after transfection.

Immunostaining of cultured astrocytes

Cells were fixed using 4 % PFA for 20 min at RT and washed in PBS. Astrocytes were subsequently permeabilized for 20 min in PBS containing 0.1 % Triton and blocked for 1 h at RT in blocking solution containing 5 % FBS in PBS. For experiments with endogenous Glt-1, astrocytes were incubated with the guinea pig anti-Glt1 (1:200) primary antibody diluted in blocking solution. To stain transfected GFP-Glt-1, astrocytes were incubated with rabbit anti-Glt1 (1:100) primary antibody [60], whereas transfected Flag-Glt-1 cells were incubated overnight with a mouse anti-Flag® primary antibody (1:200-Sigma Aldrich; #F1804) that recognized the DKK sequence. Co-stainings were performed with a rabbit (1:400) or mouse anti-GFAP (Sigma Aldrich, Cat. SAB5600060-RM246) or a rat anti-Lamp1 (1:300-Abcam; #ab25245) antibody diluted in blocking solution, respectively. The next day, cells were incubated for 1 h at RT with a mixture of anti-guinea pig Alexa Fluor 488 and anti-rabbit Alexa Fluor 568 or 544 secondary antibodies, or with a mixture of anti-mouse Alexa Fluor 568 (1:200) and anti-rat Alexa Fluor 633 in blocking solution. Nuclei were counterstained for 5 min with Hoechst (1:10000), and after washing, coverslips were mounted using Mowiol.

Fluorescence microscopy techniques

GFP-Glt-1 transfected astrocytes were imaged by Total internal reflection fluorescence microscopy (TIRFM). TIRFM was achieved with a Carl Zeiss inverted microscope equipped with an Argon laser at 37 °C using a 100×1.45 numerical aperture (NA) oil immersion objective. Green fluorescence was excited using the 488 nm laser line and imaged through a band pass filter (Zeiss) onto a Retiga SRV CCD camera. Images (12 bit, 696x520 pixel) were recorded with the same acquisition parameters (laser power, exposure time, binning) [61]. After setting the threshold, the mean intensity of the GFP signal in three randomly selected regions of interest (ROIs) was measured using ImageJ. Data were expressed as fold changes over GFP-Glt-1 intensity signal measured in Lrrk2 WT animals.

Flag-Glt-1 transfected astrocytes were imaged at 8-bit intensity resolution over 1920x1440 pixel using a Leica 5000B microscope HC PL FLUOTAR 40x/0.75 dry objective. Three ROIs/cell were defined, and the number of Glt-1 positive clusters (diameter > 1 μm) were counted manually using ImageJ.

Co-transfected Flag-Glt-1 astrocytes were imaged at 8-bit intensity resolution over

2048x2048 pixel, using a Leica SP5 confocal microscope and a HC PL FLUOTAR 40x/0.70 oil objective. After setting the threshold, ROIs were identified as the area of Lamp1, Rab11 and Rab4 and visualized in the green channel (GFP) or in the far red for the endogenous staining of Lamp1. Lamp1, Rab11 and Rab4 IntDen were calculated for each ROI. The same ROIs were then transferred to Glt-1 fluorescence channel (Red) and the IntDen was determined as a measure of Glt-1 co-localization. For the characterization of the recycling compartment, the number of GFP-Rab4-positive dots as well as the area of Rab4-positive vesicles was measured using ImageJ.

Transmission electron microscopy analysis

Primary striatal astrocytes from Lrrk2 WT and Lrrk2 G2019S mice were seeded in 35 mm dishes containing a 14 mm Gridded Coverslip (MatTek, Life Science) and co-transfected with Flag-Glt-1 and GFP-Rab4. After 48 h of transfection, cells were fixed using 4 % PFA dissolved in PBS and GFP-Rab4 was imaged on a Leica SP5 confocal microscope. Subsequently, cells were incubated in glutaraldehyde 2.5 % dissolved in 0.1 M sodium cacodylate buffer for 1 h at 4 °C and post-fixed in 1 % osmium tetroxide plus potassium ferrocyanide 1 % in 0.1 M sodium cacodylate buffer for 1 hour at 4 °C. Finally, cells were embedded in the epoxy resin (Epoxy Embedding Medium kit- Sigma Aldrich) and 70 nm-ultrathin sections were obtained using an Ultrotome V (LKB) ultramicrotome, before being processed using a Tecnai G2 transmission electron microscope (TEM) operating at 100 kV. To identify Rab4-positive structures by TEM, confocal and electron images were overlaid using nucleus shape to improve cell relocation. The diameter and area of endosomal-like structures were measured using ImageJ.

Pharmacological treatments

The following compounds were used: LRRK2 kinase inhibitor rel-3-[6-[(2R,6S)-2,6-Dimethyl-4-morpholinyl]-4-pyrimidyl]-5-[(1-methylcyclopropyl)oxy]-1H-indazole (MLi-2; 200 nM, 90 min application for the experiments on transfected cells; 120 min application for electrophysiological recordings in oocytes, Tocris; Cat. #5756) [62,63]; dibutyryl cAMP (dbcaMP; 500 µM; 10 days, ChemCruz; #B0218) [64]; PKC activator phorbol 12-myristate 13-acetate (TPA; 400 nM, 20 min, Sigma Aldrich; Cat. #SLBX8889) [64] ; PKC inhibitor Go 6976 (10 µM, 1, 10 and 90 min, Selleckchem) [65,66]; recycling inhibitor monensin (35 µM, 40 min; Sigma Aldrich; Cat. #M5273) [20]; proteasome inhibitor MG132 (20 µM, 8 hours; Sigma Aldrich; Cat. #M5273;[23]); vacuolar H^+-ATPase inhibitor bafilomycin A1 (Baf A1; 100 nM, 60 min, Selleck.EU; Cat. #S1413;[67]). For the TIRFM study as well as for the investigation of Glt-1 recycling kinetics, MLi-2

was acutely applied to Lrrk2 G2019S astrocytes 90 min prior to further pharmacological manipulations.

Image preparation and statistical analysis

All images were prepared for illustration using Adobe Illustrator CS6. Statistical analyses were performed in Prism 7 (GraphPad). Data are expressed as median with interquartile range. Gaussian distribution was assessed by D'Agostino & Pearson omnibus and Shapiro-Wilk normality tests. Data including three or more conditions were analyzed by one-way ANOVA test followed by Tukey's multiple comparisons test (Gaussian distribution) or Kruskal-Wallis test (non-Gaussian distribution) followed by Dunn's multiple comparisons test. Statistical analysis on data including two independent groups was performed with the Unpaired t-test (Gaussian distribution) or Mann-Withney test (non-Gaussian distribution). A Paired t-test (Gaussian distribution) was applied for the comparison of co-injected EAAT2+*LRRK2* G2019S oocytes before and after MLi-2 application. Levels of significance were defined as *, $, #, $p \leq 0.05$; **, $$, ##, $p \leq 0.01$; ***, $$$, ### $p \leq 0.001$.

Data availability

Data supporting the findings of the present study are available from the corresponding author, upon reasonable request.

Table 1-Sample demographics of the human cases used in this study

Cases	Sex (F/M)	Age	Post Mortem Dissection (hours)
LRRK2 G2019S 1	F	72	24.55
LRRK2 G2019S 2	F	84	32.2
LRRK2 G2019S 3	F	81	15
LRRK2 G2019S 4	F	80	44.4
Healthy Control 1	M	71	42.3
Healthy Control 2	F	82	55
Healthy Control 3	M	83	35.4
Healthy Control 4	F	80	66.2
Healthy Control 5	M	69	49.3
Healthy Control 6	F	85	37
Healthy Control 7	M	93	112
Healthy Control 8	F	91	98.5
Healthy Control 9	M	87	36
Healthy Control 10	F	68	41.5

Supplementary materials and methods

Quantitative Polymerase Chain Reaction (qPCR*)*

Total RNA was extracted from mice striata or from primary striatal astrocytes with the Total RNA Purification kit (NORGEN Biotek) and quantified by absorbance in a NanoDrop 2000c UV-Vis spectrophotometer (ThermoFisher Scientific). cDNA was synthesized with the All-in-One Cdna Synthesis SuperMix (Bimake) following manufacturer's instructions. Gene expression was quantified by qPCR in real-time PCR reactions with Sybr Green technology in a CFX96 Touch Real-Time PCR Detection System (Bio-Rad). 30 ng cDNA were used in iTaq Universal SYBR Green Supermix (Bio-Rad) at the following conditions: stage 1: 95 °C, 5 min; stage 2: 39 x (95 °C, 15 s; 60 °C, 30 s).

The primers were as follows: mSLC1A2 fw: GGTGGAAAGCCGGGACGTGGATTA; mSLC1A2 rev: GCTTGGGCATATTGTTGGCACCCT; SLC1A3 fw:

ATCCGGGAGGAGATGGTGCCCGT; SLC1A3 rev: AGGATGCCCAGAGGCGCATACCACA; ACTIN fw: TACCACCATGTACCCAGGCATT; ACTIN rev: ACTCATCGTACTCCTGCTTGCTGA; mGAPDH fw: GAGAGTGTTTCCTCGTCCCG; mGAPDH rev: ACTGTGCCGTTGAATTTGCC; TRANSFERRIN RECEPTOR fw TATAAGCTTTGGGTGGGAGGCA; TRANSFERRIN RECEPTOR rev AGCAAGGCTAAACCGGGTGTATGA;

Primers for Slc1a2, Slc1a3, β-Actin and Transferrin were purchased from Sigma Aldrich while primers for Gapdh were purchased from Metabion International AG. The quantification of the gene relative expression was carried out by the Delta-Delta Ct method [68] by normalizing to the reference genes Gapdh, β-Actin and Transferrin receptor. A dissociation curve was built in the 60-95 °C range to confirm the specificity of the amplification product.

Results

Severe deficits in EAAT2 levels and increased gliosis in the post-mortem basal ganglia of LRRK2 G2019S PD patients

To investigate the role of EAAT2 in the pathophysiology of LRRK2-PD, we first examined the presence of the glutamate transporter protein in the basal ganglia of LRRK2 G2019S PD patients and age-matched controls by western blot (Fig.1A). Consistent with previous reports, the EAAT2 antibody recognized multiple bands corresponding to the monomeric (60 KDa), and multimeric, SDS-resistant (180 KDa) conformations [69-71]. An additional 250 KDa band was detected which is compatible with EAAT2 multimers [72,73] (Fig.1A). We determined the total amount of the transporter by combining the densitometry of the three bands (Fig.1B) as well as we quantified the three bands separately (Supplementary Fig.1 A-C). In all cases band intensity was normalized to the housekeeping protein GAPDH. We observed that EAAT2 protein was nearly absent in the basal ganglia of LRRK2 G2019S PD patients as compared to healthy controls (Fig.1B; LRRK2 G2019S PD patient cases vs age-matched controls; p=0.004), and this difference affected both the multimeric and monomeric fractions (Supplementary Fig. 1A-C; LRRK2 G2019S PD patients vs age-matched controls: a, p=0.0160; b, p=0.0114; c, p=0.0168). EAAT2 is highly expressed by astrocytes [4]. Therefore, to determine whether the decreased expression of EAAT2 was due to a lower number of astrocytes in LRRK2 G2019S PD patients, we assessed the amount of the cytosolic marker glutamine synthetase (GS), since its expression is restricted to astrocytes and does not depend on their activation status (Fig.1A). GS expression levels in the basal ganglia were comparable between LRRK2 G2019S PD patients and age-matched controls (Fig.1C; LRRK2 G2019S PD patients vs controls, p=0.227). However, expression levels of GFAP (a marker for astrogliosis) were significantly increased in the basal ganglia of LRRK2 G2019S PD patients as shown in Fig.1D-F (D, LRRK2 G2019S PD patients vs age-matched controls; p=0.044). Moreover, immunohistochemical detection of GFAP-positive cells showed that astrocytes in the basal ganglia of LRRK2 G2019S PD patients were abundant (Fig. 1E-F, arrows) and adopted the typical morphology of hyperactive cells, with enlarged and densely stained cytoplasm (Fig. 1E-F, insets). Taken together, these data show a significant decrease in the expression of the glutamate transporter EAAT2 in the basal ganglia of LRRK2 G2019S PD patients and the reduction of EAAT2 is associated with increased astrogliosis.

Glutamate transporter expression and functionality are perturbed in the striatum of young Lrrk2 G2019S mice

To inquire whether deficits in glutamate transporter expression occur before dopaminergic degeneration, we compared the expression of Glt-1, the mouse equivalent of EAAT2, in the striatum of 4-month-old Lrrk2 WT and Lrrk2 G2019S knock-in mice. As previously reported, we confirmed the presence of two bands, corresponding to Glt-1 monomers (60 KDa) and Glt-1 multimers (180 KDa), respectively (Fig. 2A) [69-71]. Lrrk2 G2019S mice presented a decrease in the total amount of Glt-1 as compared to Lrrk2 WT controls (Fig.2B, Lrrk2 WT vs G2019S; p=0.008). When analyzing the two bands separately, the lower Glt-1 band also showed a significant decrease in the Lrrk2 G2019S mice, even though levels of the higher band did not reach statistical significance (Supplementary Fig. 1D, Lrrk2 WT vs Lrrk2 G2019S; p=0.0175; Supplementary Fig. 1E, Lrrk2 WT vs Lrrk2 G2019S; p=0.07).

We next performed qPCR analyses to explore whether the decrease in Glt-1 protein levels was attributed to a decrease of its mRNA levels in the striatum. Importantly, no significant changes in mRNA levels between genotypes were detected for the two main glutamate transporters Glt-1 (Supplementary Fig.1F, Lrrk2 WT vs Lrrk2 G2019S; p=0.99) or the glutamate/aspartate transporter (Glast), which is the second most important astrocytic glutamate transporter (Supplementary Fig.1F, Lrrk2 WT vs Lrrk2 G2019S; p=0.6575). Similar to what we observed in human samples, GS protein levels were comparable between the genotypes (Fig.2C, Lrrk2 WT vs G2019S, p=0.1411), while there was an increase in the levels of GFAP (Fig.2D, Lrrk2 WT vs Lrrk2 G2019S; p<0.0001), suggesting enhanced gliosis in young Lrrk2 G2019S mice. Immunofluorescence imaging confirmed a reduction of Glt-1 staining in the striatum of Lrrk2 G2019S mice compared to controls (Fig.2F). Quantifications of the integrated fluorescence intensity (IntDen) of GFAP (Fig.2G; Lrrk2 WT vs Lrrk2 G2019S, p=0.0001) and of the number of GFAP-positive astrocytes (Fig.2H; Lrrk2 WT vs Lrrk2 G2019S, p=0.1) further indicate that decreased Glt-1 levels correlate with an intense astrogliosis in Lrrk2 G2019S mice. Tyrosine Hydroxylase (TH) levels as quantified by western blot from the same mice revealed no signs of dopaminergic cell loss, indicating that the decrease in Glt-1 levels seems to precede neurodegenerative events (Fig.2E, Lrrk2 WT vs Lrrk2 G2019S, p=0.39).

To dissect the Lrrk2-mediated effects on glial Glt-1 levels, we isolated primary striatal astrocytes from Lrrk2 WT and Lrrk2 G2019S mice. Astrocytes were treated with dbcAMP to stimulate endogenous Glt-1 expression [74]. Consistent with published data [75], qPCR analysis showed a more than 10-fold increase in Glt-1 mRNA levels upon dbcAMP treatment (Supplementary Fig.1G). Immunocytochemistry revealed that Glt-1 was diffusely expressed in Lrrk2 WT astrocytes, while Lrrk2 G2019S astrocytes displayed a less pronounced staining, almost restricted to discrete dots (Fig. 2I, arrowheads).

To evaluate whether the Glt-1 deficits and impaired Glt-1 localization may functionally affect glutamate re-uptake in astrocytes, we purified striatal mouse gliosomes from Lrrk2 WT and Lrrk2 G2019S mice. Gliosomes constitute pure subcellular *ex-vivo* preparations that resemble most of the molecular and functional features of astrocytes *in vivo* [51,53]. [^{3}H]D-Asp, a non-metabolizable analogue of glutamate used to mimic the endogenous neurotransmitter [76], was applied to assess Glt-1 activity, and experiments were conducted in the presence of 10 μM UCPH-101 to exclude [^{3}H]D-Asp uptake by Glast. To calculate the K_m and the V_{max} of [^{3}H]D-Asp uptake, radioactivity was determined in gliosomes in the presence of different concentrations of [^{3}H]D-Asp. As shown in Fig. 2J, Lrrk2 G2019S-derived gliosomes displayed a lower V_{max} of aspartate uptake as compared to age-matched Lrrk2 WT mice (Fig. 2l, V_{max} [Lrrk2 WT]: 6.7±1.37 nmol/mg/2 min, V_{max} [Lrrk2 G2019S]: 2.73±0.59 nmol/mg/2 min, p= 0.036), while no significant difference was registered in the K_m values (Fig. 2J; K_m [Lrrk2 WT] 2.56±0.16 mM, Km [Lrrk2 G2019S] 2.05±0.14 mM, p=0.054). Altogether these findings show that, similar to what we observed with human samples, astrocytes from Lrrk2 G2019S mice present a reduced expression of Glt-1, which results in reduced glutamate uptake and is associated with increased gliosis.

Human pathogenic G2019S LRRK2 mutation impacts on EAAT2 electrophysiological properties

To confirm that the reduced glutamate uptake observed in Lrrk2 G2019S gliosomes also applies to the human EEAT2 protein, we used *Xenopus laevis* oocytes, an excellent model system to study transport processes on a cellular level [77]. Human glutamate transporter EAAT2 mRNA was co-injected with human LRRK2 WT or LRRK2 G2019S mRNA in oocytes, and two-electrode voltage-clamp was performed to record the transport current elicited by glutamate through EAAT2 (Experimental design in Fig.3A). The inward transport associated-current (I_{EAAT2}) obtained upon the application of glutamate to oocytes injected with LRRK2 G2019S mRNA was significantly reduced as compared to the one obtained from oocytes injected with LRRK2 WT mRNA (Fig. 3B; EAAT2+LRRK2 WT: mean amplitude 43±3 nA vs EAAT2+LRRK2 G2019S: mean amplitude 25±2 nA; p<0.0001). We also measured the maximal transport current (I_{max}) and the apparent affinity for glutamate (aK_m). We found that the expression of LRRK2 G2019S mRNA significantly decreased the I_{max} but not the aK_m of the transporter as compared to the WT counterpart (Fig. 3C; EAAT2+LRRK2 G2019S, aK_m: 51±27 μM, I_{max}: 28±3 nA vs EAAT2+LRRK2 WT, aK_m: 89±32 μM, I_{max}: 52±5 nA; aK_m, p =0.05; I_{max}, p<0.001).

We next imaged EAAT2 in oocyte slices to understand the reduction of transport current observed in the presence of LRRK2 G2019S. Fluorescence images and IntDen quantification

revealed that the transporter was mainly found at the plasma membrane in oocytes injected with LRRK2 WT, while it was sparsely localized upon pathogenic LRRK2 G2019S expression (Fig.3D-E, EAAT2+LRRK2 WT vs EAAT2+LRRK2 G2019S, p=0.001). Importantly, short-term incubation of LRRK2 G2019S-injected oocytes with the LRRK2 kinase inhibitor MLi-2 restored both the localization (Fig. 3D-E; EAAT2+LRRK2 G2019S vs EAAT2+LRRK2 G2019S+MLi-2, p=0.0005) and the activity of the transporter (Fig. 3F; EAAT2+LRRK2 G2019S, mean amplitude 17±1 nA vs EAAT2+LRRK2 G2019S+MLi-2 mean amplitude 37±3 nA; p<0.0001; EAAT2+LRRK2 WT: mean amplitude 34±4 vs LRRK2 G2019S+MLi-2; p=0.715). Together with our findings on mouse gliosomes, these observations suggest that the presence of pathogenic human LRRK2 G2019S does not alter the catalytic properties of the glutamate transporter. However, the mutation affects the amount of glutamate transporter functionally trafficked to/from the plasma membrane in a manner mediated by the kinase activity.

LRRK2 G2019S influences Glt-1 interactome

We next performed an unbiased protein-protein interaction screen to gain insights into the mechanism behind the mutant LRRK2-dependent Glt-1 mislocalization and reduced protein levels. Endogenous Glt-1 was immunoprecipitated from homogenized WT and Lrrk2 G2019S mouse striata (Fig. 4A). As negative control, only magnetic beads were incubated with WT and Lrrk2 G2019S solubilized brain extracts, respectively. Glt-1 interactors were revealed using liquid-chromatography coupled with tandem mass spectrometry (LC-MS/MS) (Supplementary file 1). The two interactome datasets were compared to highlight significant differences in protein abundances (Supplementary file 2). Common and divergent Glt-1 binders between the Lrrk2 WT and G2019S genetic environments were identified upon filtering hits with fold-change >3.5 with respect to the relative control. As shown in Figure 4, 40 interactors were present in both datasets, 14 were unique to Glt-1 immunoprecipitated from Lrrk2 WT background and 10 were unique to Lrrk2 G2019S background (Fig. 4B). Gene Ontology (GO) analysis was employed to identify discrete functional enrichments, and data relative to the Cellular Component (CC) biological domain were analyzed in detail (Supplementary file 3). In both datasets Glt-1 was in contact with membrane domains (GO:0045121; GO:0098857), synaptic and vesicular components (GO:0045202; GO:0043232), cytoskeletal scaffolds (GO:0005856; GO:0005874) and mitochondrial elements (GO:0005743; GO:0031966; GO:0005740) (Fig.4c) as already reported in [71]. Among the GO terms that characterize the transporter in the Lrrk2 G2019S genotype, we observed several unique categories associated with internalized vesicles and clathrin-mediated endocytosis (GO:0030119; GO:0030128) (Fig.4C). Conversely, components of the plasma membrane region associated with

sodium-potassium exchanging ATPase complexes were represented in the Lrrk2 WT genotype only (GO:0098796; GO:0098590; GO:0005890) (Fig.4c). Taken together, these data indicate that the pathogenic Lrrk2 G2019S mutation changes the interactome of endogenous striatal Glt-1 toward specific components of the endo-vesicular pathways.

Glt-1 displays an altered localization in Lrrk2 G2019S astrocytes

Having collected robust evidence that the G2019S mutation affects endogenous Glt-1 cellular localization, we next employed primary striatal astrocytes acutely transfected with a GFP-Glt-1 construct to examine transporter trafficking events. TIRFM imaging was performed to selectively visualize Glt-1 localization within thin regions of the plasma membrane [61]. We observed that GFP-Glt-1 localized in or immediately below the plasma membrane in Lrrk2 WT astrocytes, showing a sparse 'patchy' pattern (Fig.5A – WT inset). Although showing a similar membrane distribution, Glt-1 was less detectable on the cell surface of Lrrk2 G2019S astrocytes (Fig.5A – GS inset). The quantification of Glt-1 mean fluorescence using TIRFM confirmed a lower presence of Glt-1 at the plasma membrane of Lrrk2 G2019S astrocytes as compared to Lrrk2 WT astrocytes (Fig.5B, Lrrk2 WT vs Lrrk2 G2019S, $p<0.0001$).

By imaging the total amount of GFP-Glt-1 using epifluorescence microscopy, we detected a clear accumulation of Glt-1 in round intracellular clusters along with the spotted membrane distribution in Lrrk2 G2019S astrocytes (Fig.5D). Glt-1 was present within two distinct populations of clusters, namely a larger cluster of ~1.8 μm diameter and a smaller cluster of ~0.8 μm (Supplementary Fig.2A,C). In contrast, a unique population of dots with an average diameter of 0.6 μm was present in the Lrrk2 WT background, perhaps reflecting clusters in the plasma membrane (Supplementary Fig.2A-B). Using intracellular cluster formation as a readout (diameter>1μm), we detected a significant increase of Glt-1 clusters in Lrrk2 G2019S astrocytes compared to the Lrrk2 WT genotype (Fig.5D-E Lrrk2 WT vs Lrrk2 G2019S, $p<0.0001$). Noteworthy, 90 min MLi-2 application restored the number of Glt-1-positive clusters to control values (Fig.5D-E; Lrrk2 G2019Svs Lrrk2 G2019S+MLi-2, $p=0.002$; Lrrk2 G2019S+MLi-2 vs Lrrk2 WT, $p>0.99$). To investigate a possible role for LRRK2 in PKC-mediated internalization of Glt-1, we used the PKC activator TPA, as well as the PKC inhibitor Go 6976 (Fig.5C). In agreement with published data [19,64], the application of TPA enhanced Glt-1 intracellular clusters in Lrrk2 WT astrocytes (Fig.5D-E; Lrrk2 WT vs Lrrk2 WT+TPA, $p=0.009$). Of note, the distribution of cluster diameters in this condition peaked ~1.9 μm, which is similar to that observed in Lrrk2 G2019S astrocytes (Supplementary Fig.2A,D). No significant changes were observed in the number of Glt-1-positive puncta in Lrrk2 G2019S astrocytes upon TPA treatment, suggesting that the majority of Glt-1 was

localized to the intracellular compartment already under basal conditions (Fig.5 D-E; Lrrk2 G2019S vs Lrrk2 G2019+TPA, p>0.99). To unravel whether Lrrk2 acts upstream of PKC, we applied MLi-2 to TPA-treated Lrrk2 WT astrocytes. Interestingly, the application of MLi-2 did not restore the number of Glt-1 clusters to basal values (Fig.5 D-E; Lrrk2 WT vs Lrrk2 WT+TPA+MLi-2, p<0.0001). Moreover, PKC inhibition using Go 6976 did not prevent Glt-1 clustering in Lrrk2 G2019S astrocytes (Fig.5D-E; Lrrk2 G2019S vs Lrrk2 G2019S+Go 6976, p>0.99). These data demonstrate that Lrrk2 G2019S reduces Glt-1 localization at the plasma membrane in a PKC-independent manner in primary astrocytes. Moreover, the correction of the pathogenic phenotype observed upon application of MLi-2, indicates that the Lrrk2 kinase activity is crucial for the relocation of Glt-1.

Glt-1 is retained at the Rab4-positive compartment in Lrrk2 G2019S striatal astrocytes

To determine the identity of the Glt-1 clusters, we co-transfected Lrrk2 WT and Lrrk2 G2019S astrocytes with Flag-Glt-1 together with GFP-Lamp1 (lysosomal marker), GFP-Rab11 (marker of slow-recycling endocytosis) or GFP-Rab4 (marker of fast-recycling endocytosis) (Fig. 6A). Quantification analyses showed that there was no significant difference in the amount of Lamp1, Rab11 or Rab4 fluorescence between the two genotypes (Fig.6B,D,F; all comparisons p>0.05). We then quantified the co-localization of Glt-1 with the three markers. There were no significant changes in the amount of the transporter in the Lamp1- or Rab11-positive compartments in Lrrk2 G2019S astrocytes as compared to Lrrk2 WT astrocytes (Fig. 6C,E; all comparisons p>0.05). However, there was a significant increase in the amount of Glt-1 co-localizing with the Rab4-positive fast-recycling vesicles in Lrrk2 G2019S astrocytes as compared to control (Fig.6G, Lrrk2 WT vs Lrrk2 G2019S, p=0.001). Interestingly, short-term application of MLi-2 reverted the Lrrk2 G2019S-mediated pathogenic phenotype as shown by the loss of co-localization between Glt-1 and Rab4-positive vesicles (Fig. 6G, Lrrk2 G2019S vs Lrrk2 G2019S+MLi-2, p=0.001; Lrrk2 G2019S +MLi-2 vs Lrrk2 WT, p=0.98). Z-stacks orthogonal projections confirmed that Glt-1 co-localized with Rab4-positive vesicles in Lrrk2 G2019S primary astrocytes (Supplementary Fig.3A).

Since pathogenic Lrrk2 did not influence the expression of Rab4 protein *per se*, we investigated the impact of the kinase on Rab4-positive vesicle morphology using both confocal fluorescence microscopy and TEM (Fig.6H,K). Fluorescence analysis demonstrated that the Lrrk2 G2019S mutation did not alter the total amount of Rab4-positive vesicles (Fig. 6I, Lrrk2 WT vs Lrrk2 G2019S, p>0.05). Rather, the area of Rab4-positive fast recycling endosomes was significantly enhanced in the presence of the pathogenic Lrrk2 mutation (Fig. 6J, Lrrk2 WT vs Lrrk2 G2019S, p=0.0032). By overlapping fluorescence images with TEM ultrathin sections, we

were able to identify and define the Rab4-positive recycling vesicles (Supplementary Fig.3B-asterisks). Rab4-positive endosomes presented an irregular shaped vacuole (0.2-0.5 μm diameter) characterized by an electron-lucent lumen [78,79]. TEM analysis confirmed that the Lrrk2 G2019S mutation markedly increased the area of Rab4-positive vesicles (Fig.6K,L; Lrrk2 WT vs Lrrk2 G2019S, p>0.0001) as compared to controls. Overall, we show here that in Lrrk2 G2019S astrocytes the transporter is predominantly confined to defective, enlarged Rab4-positive recycling vesicles. Also in this case, the rescuing effect of MLi-2 suggests that the dysregulation of Lrrk2 kinase activity is sufficient to impair Glt-1 trafficking.

Lrrk2 G2019S perturbs Glt-1 recycling and favors its degradation

We next examined whether Glt-1 accumulation in the Rab4-positive compartment in the Lrrk2 G2019S astrocytes was due to a delay in recycling. First, we applied the recycling inhibitor Monensin on primary striatal Lrrk2 WT and G2019S astrocytes and investigated the co-localization of Glt-1 with Rab4 (Fig. 7A). In untreated cells, Glt-1 accumulated in Rab4-positive recycling vesicles in the presence of the Lrrk2 pathogenic mutation as compared to controls (Fig.7B; untreated Lrrk2 WT vs untreated Lrrk2 G2019S, p=0.003). Monensin application induced a significant accumulation of Glt-1 in Rab4-positive vesicles in Lrrk2 WT cells (Fig. 7B; untreated Lrrk2 WT vs Lrrk2 WT+Monensin, p=0.001), thereby phenocopying the distribution of the transporter observed in untreated Lrrk2 G2019S astrocytes (Fig. 7B; Lrrk2 WT+Monensin vs untreated Lrrk2 G2019S, p>0.99). Conversely, Monensin treatment did not induce further Glt-1 accumulation in Rab4-positive vesicles in the Lrrk2 G2019S astrocytes (Fig. 7B; untreated Lrrk2 G2019S vs Lrrk2 G2019S+Monensin, p>0.99), suggesting that the transporter was almost completely incorporated in the fast-recycling compartment under basal conditions in those cells.

We next studied the recycling kinetics by measuring Glt-1 localization in Rab4-positive vesicles after TPA-induced internalization. To isolate the unique contribution of the recycling pathway, the subsequent basal internalization was blocked using Go 6976. We again confirmed that under basal conditions Glt-1 accumulated as clusters in Rab4-positive vesicles in Lrrk2 G2019S but not in Lrrk2 WT astrocytes (Fig.7 C-D; Lrrk2 WT vs Lrrk2 G2019S, p=0.01), and that the application of MLi-2 reverted this phenotype (Fig.7 C-D; Lrrk2 G2019S vs Lrrk2 G2019S+MLi-2, p=0.002; Lrrk2 G2019S+MLi-2 vs Lrrk2 WT, p= 0.79). Upon TPA stimulation, there was an overall increase of Glt-1 in Rab4-positive vesicles in Lrrk2 WT and Lrrk2 G2019S+MLi-2 astrocytes, reaching values of Glt-1/Rab4 co-localization similar to those observed in Lrrk2 G2019S astrocytes (Fig.7 C-D; Lrrk2 WT+TPA vs Lrrk2 G2019S+TPA, p=0.63; Lrrk2 G2019S+TPA vs Lrrk2 G2019S+MLi-2+TPA, p=0.99; Lrrk2 WT+TPA vs Lrrk2 G2019S+MLi-2+TPA, p=0.70).

Conversely, the amount of Glt-1 co-localizing with Rab4-positive vesicles in Lrrk2 G2019S astrocytes did not increase upon TPA stimulation (Fig.7 C-D). Both Lrrk2 WT and Lrrk2 G2019S+MLi-2 astrocytes displayed a significant decrease of Glt-1 in Rab4-positive vesicles already 1 min after Go 6976 application (Fig.7 C-D; Lrrk2 WT+ Go T1' vs Lrrk2 G2019S+MLi-2+Go T1', p=0.88; Lrrk2 WT+ Go T1' vs Lrrk2 WT, p=0.95; Lrrk2 G2019S+MLi-2+Go T1' vs Lrrk2 G2019S+MLi-2, p>0.99). In contrast, Glt-1 was almost entirely retained in Rab4 vesicles in Lrrk2 G2019S astrocytes at this time point (Fig.7 C-D; Lrrk2 WT+ Go T1' vs Lrrk2 G2019S+Go T1', p=0.01; Lrrk2 G2019S+MLi-2+Go T1' vs Lrrk2 G2019S+Go T1', p=0.007; Lrrk2 G2019S+Go T1' vs Lrrk2 G2019S, p=0.64). A most prominent effect was observed 10 min after Go 6976 application (Fig.7 C-D; Lrrk2 WT+ Go T10' vs Lrrk2 G2019S+Go T10', p=0.03; Lrrk2 G2019S+MLi-2+Go T10' vs Lrrk2 G2019S+Go T10', p=0.06; Lrrk2 WT+ Go T10' vs Lrrk2 G2019S+MLi-2+Go T10', p=0.95; Lrrk2 WT+ Go T10' vs Lrrk2 WT, p=0.39; Lrrk2 G2019S+MLi-2+Go T10' vs Lrrk2 G2019S+MLi-2, p=0.99). Although not reaching statistical significance, the overall amount of the transporter at the Rab4-positive organelles progressively decreased in the pathogenic LRRK2 astrocytes upon Go treatment (Fig.7 C-D; Lrrk2 G2019S+ Go T10' vs Lrrk2 G2019S, p=0.49). Of note, this phenomenon was not associated with a relocation of Glt-1 to the plasma membrane in the G2019S background (Fig.7C, arrowheads).

Therefore, we examined whether Glt-1 incorporated into Rab4-positive vesicles was targeted for degradation in the Lrrk2 G2019S astrocytes. As Glt-1 can be degraded through both the proteasome [23,24] and the lysosome [18,22], we monitored the presence of Glt-1 in the fast recycling and lysosomal compartments in the presence of either MG132 or Bafilomycin to block proteasomal or lysosomal function, respectively [23,67]. Lrrk2 WT and G2019S astrocytes were co-transfected with Flag-Glt-1 and GFP-Rab4, and stained for the endogenous lysosomal protein Lamp1 to measure Glt-1 localization in the Rab4- and Lamp1-positive organelles (Fig.7E). Glt-1 preferentially accumulated in the Rab4-positive rapid recycling compartment in the Lrrk2 G2019S astrocytes as compared to control cells (Fig.7F; Lrrk2 WT and Lrrk2 G2019S; p=0.02), whilst a comparably low distribution of Glt-1 to the lysosomal compartment was observed in both genotypes under basal conditions (Fig.7G Lrrk2 WT and Lrrk2 G2019S; p>0.99). Proteasome inhibition did not significantly enhance the fraction of Glt-1 co-localizing with the Rab4-positive compartment in Lrrk2 G2019S astrocytes (Fig.7F; Lrrk2 G2019S vs Lrrk2 G2019S+MG132; p=0.067), and promoted only a slight increase of Glt-1 localization in the lysosomal compartment in Lrrk2 G2019S astrocytes (Fig.7G; Lrrk2 G2019S vs Lrrk2 G2019S+MG132; p=0.038). In contrast, whilst lysosomal inhibition did not cause a significant increase of Glt-1 in the Rab4-positive compartment in Lrrk2 G2019S astrocytes (Fig.7F; Lrrk2 GS and Lrrk2 G2019S+Bafilomycin; p=0.11), it

dramatically accentuated Glt-1 accumulation in the lysosomal vesicles in the Lrrk2 G2019S astrocytes (Fig.7G; Lrrk2 G2019S vs Lrrk2 G2019S+Bafilomycin; p=0.0001). These results indicate that pathogenic Lrrk2 profoundly perturbs Glt-1 recycling to the cell membrane, possibly associated with the re-routing of the transporter for lysosomal degradation (Fig. 7H).

Discussion

In the present study, we reported that EAAT2 is nearly absent in *post-mortem* basal ganglia from Parkinson's disease (PD) patients carrying the LRRK2 G2019S mutation. These results corroborate previous clinical data showing alterations in the glutamate content in the brain as well as in the plasma of sporadic PD patients [31,32,34,80,81]. Striatal EAAT2 downregulation correlated with increased expression of the reactive marker GFAP in basal ganglia glial cells of LRRK2-linked PD patients. Although impaired glutamate buffering is often found accompanied by astroglial reactivity and neuroinflammation in several disease models [10,82,83], conflicting results have been published in the context of PD patients. Enhanced GFAP reactivity has been clearly documented in *Substantia Nigra pars compacta (SNpc)* and olfactory bulbs [84-86]. However, one report suggested astrocytic atrophy (instead of reactivity) in PD brains, since low levels of astrocyte markers were observed in the *SNpc* and the striatum [84], and studies in human iPS-derived astrocytes from LRRK2 G2019S-PD patients suggested a similar mechanism [87]. Our study suggests absence of astrocyte degeneration or atrophy since the levels of the astrocyte marker GS were not perturbed in the context of disease. Accordingly, the presence of astrocyte reactivity has been reported in different transgenic mice overexpressing the LRRK2 G2019S kinase [88,89].

Lrrk2 G2019S knock-in mice display an evident phenotype characterized by a significant downregulation of striatal Glt-1 protein levels and extensive astrogliosis, which recapitulates the human disease in *post-mortem* basal ganglia. Thus, the knock-in G2019S mouse is an outstanding model system to unravel the mechanism that links pathogenic Lrrk2 to transporter deficiencies. Glt-1 deficits in mice appear without any nigral degeneration, indicating that Lrrk2-mediated glutamate transporter dysfunction in the striatum might anticipate dopaminergic cell loss. In agreement with the downregulation of Glt-1 protein, an enhanced glutamatergic cortico-striatal neurotransmission has been described in this animal model [43,44]. These findings suggest that striatal glutamatergic imbalance and correlated glutamate-induced excitotoxicity intervene in PD pathophysiology.

LRRK2 is expressed in glial cells and plays a relevant role in astrocyte physiology both in human and mouse [59,90-92]. In this context, we specifically dissected the contribution of the pathogenic Lrrk2 mutation on Glt-1 functionality in astrocytes at endogenous levels in cultured cells as well as in pure subcellular astrocytic *ex vivo* preparations. In primary striatal cells, we confirmed a reduced level of the transporter, in agreement with our observations in human and murine striatal lysates. These observations fit with the functional analysis carried out on isolated

mouse striatal gliosomes, which reveal a decreased ability of the transporter to reuptake glutamate. By comparing the kinetic values, we find that Lrrk2 G2019S impinges on Glt-1 transport velocity without affecting substrate affinity. Similarly, the expression of human LRRK2 G2019S induces a decrease of the EAAT2 transport current without modifying the biophysical properties of the transporter in *Xenopus* oocytes. Therefore, the EAAT2/Glt-1 functional impairment can be ascribed to a reduced localization of the transporter at the plasma membrane mediated by LRRK2. Importantly, the LRRK2 G2019S effects on EAAT2 are restored upon acute inhibition of the G2019S kinase activity by MLi-2, indicating that pathogenic LRRK2 impairs proper EAAT2 homeostasis.

Endogenous Glt-1 interacts with partially different protein environments in the two backgrounds as revealed by mass spectrometry data. On one hand, striatal Glt-1 immunoprecipitated from Lrrk2 WT mice mainly interacts with membrane proteins. In agreement with previous findings, we identified the Na^+-K^+ pump as a Glt-1 interactor in a Lrrk2 WT background, confirming that Glt-1 and Na^+-K^+-ATPases are part of the same macromolecular complex and operate as a functional unit to regulate physiological glutamatergic neurotransmission [93]. On the other hand, Glt-1 almost exclusively interacts with intracellular proteins in presence of the G2019S mutation. Among those proteins, we identified proteins involved in the endo-vesicular pathway, suggesting a different subcellular compartmentalization of the transporter in the presence of the Lrrk2 G2019S mutation.

It has been consistently reported that Glt-1 continuously exchanges between diffuse and spotted localization at the surface, shaping synaptic transmission [15,16]. Moreover, Glt-1 undergoes basal PKC-mediated endocytosis and intracellular cluster formation in astrocytic processes to regulate glutamate uptake activity [64]. In our system, only the amount of the transporter, but not the spotted distribution at the plasma membrane, was affected by pathogenic Lrrk2. Conversely, Lrrk2 G2019S astrocytes exhibited the presence of large intracellular Glt-1 clusters resembling, in terms of dimension, those found upon pharmacological stimulation of PKC-mediated endocytosis of Glt-1. However, our data exclude the involvement of Lrrk2 in the PKC-mediated internalization pathway. Indeed, the inhibition of Lrrk2 kinase activity was not able to revert the PKC-induced clusterization in control astrocytes, and PKC inhibition failed to reduce Glt-1 clusters in G2019S astrocytes. PKC activation was also not able to induce a further increase in Glt-1 clusters in Lrrk2 G2019S astrocytes, suggesting that almost all of the transporter is internalized in the pathogenic Lrrk2 background.

In agreement with multiple reports suggesting a role for Lrrk2 in endocytic recycling events ([47,94], biorXiv, doi: 10.1101/2020.07.27.219501), we here demonstrate that Lrrk2 operates in Glt-1 recycling to the plasma membrane. In the LRRK2 G2019S astrocytes, Glt-1 is preferentially engulfed in fast-recycling endosomes, which are recognized by overexpression of the marker Rab4. Pharmacological Lrrk2 inhibition reduces the amount of Glt-1 co-localizing with the Rab4-positive marker and promotes Glt-1 redistribution to the plasma membrane, which allows for the functional recovery of the transporter as assessed by electrophysiological recordings in oocytes. By combining confocal and TEM ultrastructural analysis, we show that the Lrrk2 G2019S mutation profoundly affects the architecture of the fast-recycling Rab4-positive organelles in astrocytes, promoting an enlargement of the area of these vesicles. In this regard, our group recently reported a loss of function of Annexin A2 (AnxA2) in Lrrk2 G2019S astrocytes [59]. AnxA2 is a protein involved in sorting endosome maturation and recycling endosome formation [59,95,96]. Although further studies are warranted, AnxA2 deficits may be at least in part responsible for the enlarged size of the Rab4-positive endosomal recycling structures reported here.

The role of Lrrk2 in Glt-1 recycling was further dissected by pharmacological approaches. The accumulation of Glt-1 in the Rab4-positive compartment observed in Lrrk2 G2019S astrocytes was phenocopied by blocking the recycling of Glt-1 in control astrocytes. In Lrrk2 G2019S astrocytes, the same treatment did not induce further increases in Glt-1 co-localization with Rab4 vesicles, confirming that almost the totality of the transporter is incorporated in this subcellular compartment under basal conditions. Moreover, our observations on the kinetics of the process confirm that when internalized, Glt-1 is re-routed to early endosomes, as reported in [17]. While Glt-1 repopulates the plasma membrane in Lrrk2 wild-type astrocytes, Glt-1 is basally captured and persists in the Rab4 compartment in the pathogenic Lrrk2 context. In addition, a tendential decrease in the amount of Glt-1 colocalizing with the Rab4-positive marker not associated with plasma membrane re-localization indicates that the persistent delay in Glt-1 recycling might promote the degradation of the protein. Accordingly, blockade of the degradative systems in the pathogenic Lrrk2 background promoted an increase in the amount of Glt-1 colocalizing with a Lamp1-positive compartment upon both proteasomal and, especially, lysosomal inhibition.

In conclusion, our work reveals that the Lrrk2 G2019S mutation profoundly affects Glt-1 recycling to the plasma membrane by impinging on the early endosomal fast recycling compartment in striatal astrocytes. Although additional mechanistic investigations are needed, we propose that

the cellular degradative system may eventually promote Glt-1 turnover by sensing the overload of the transporter in the Rab4-positive compartment (Fig. 7H). In this manner, a chronic, subtle LRRK2-mediated impairment of the recycling machinery in brain cells might cause a progressive depletion of Glt-1 with a consequent reduction of extracellular glutamate clearance.

In a broader context, our work supports a novel pathogenic mechanism by which the nigro-striatal synapses might be affected at the early stage of the neurodegenerative process. Indeed, the LRRK2-mediated impairment of the astrocytic glutamate reuptake capacity could induce a premature striatal glutamate accumulation, anticipating subsequent irreversible consequences on the integrity of dopaminergic connections.

Author contribution

L.I. and L.C. designed the study, optimized and performed experiments, interpreted data, and wrote the manuscript; V.G. performed imaging experiments and helped in preparing primary astrocyte cultures; F.P. and G.P. performed qPCR experiments; E.Gi. and N.P. contributed to data analysis; A.M., T.B. and G.B. performed gliosomes experiments; I.B. and G.A. performed mass spec experiments; A.D.I., C.R. and E.B. performed electrophysiological experiments; A.M. and C.P. performed TIRFM experiments; R.B. provided human samples; E.Gi., L.B., E.Gr. and S.H. have contributed to manuscript editing and optimization. All authors have read and approved the final manuscript.

Acknowledgments

The Authors thank the University of Padova to support L.C. as assistant professor and the IRCCS San Camillo Hospital, Venice, Italy. This work was supported by UniPD (STARs 2019: Supporting TAlents in ReSearch) and the Italian Ministry of Health (GR-2016-02363461) to L.C. L.I. is a post-doctoral fellow supported by UniPD. G.P. is supported by Fondazione Telethon (grant TDPG00514TA), MIUR (PRIN-2017ENN4FY), and Fondazione Cariplo (project 2019-3415). F.P. received support by Fondazione Caritro (project 2019.0230). R.B. is funded by Reta Lila Weston Institute and the British Neuropathological Society. S.H. is funded by the MJFF and by intramural funds from Rutgers University. We thank Raffaella Cinquetti for the technical support to the electrophysiological experiments.

Competing interests

The Authors have no conflicts of interest to declare.

References

1. Murphy-Royal C, Dupuis J, Groc L, Oliet SHR. Astroglial glutamate transporters in the brain: Regulating neurotransmitter homeostasis and synaptic transmission. *J Neurosci Res*. Nov 2017;95(11):2140-2151. doi:10.1002/jnr.24029
2. Verkhratsky A, Nedergaard M. Physiology of Astroglia. *Physiol Rev*. Jan 1 2018;98(1):239-389. doi:10.1152/physrev.00042.2016
3. Malik AR, Willnow TE. Excitatory Amino Acid Transporters in Physiology and Disorders of the Central Nervous System. *Int J Mol Sci*. Nov 12 2019;20(22)doi:10.3390/ijms20225671
4. Furness DN, Dehnes Y, Akhtar AQ, et al. A quantitative assessment of glutamate uptake into hippocampal synaptic terminals and astrocytes: new insights into a neuronal role for excitatory amino acid transporter 2 (EAAT2). *Neuroscience*. Nov 11 2008;157(1):80-94. doi:10.1016/j.neuroscience.2008.08.043
5. Roberts RC, Roche JK, McCullumsmith RE. Localization of excitatory amino acid transporters EAAT1 and EAAT2 in human postmortem cortex: a light and electron microscopic study. *Neuroscience*. Sep 26 2014;277:522-40. doi:10.1016/j.neuroscience.2014.07.019
6. Danbolt NC, Furness DN, Zhou Y. Neuronal vs glial glutamate uptake: Resolving the conundrum. *Neurochem Int*. Sep 2016;98:29-45. doi:10.1016/j.neuint.2016.05.009
7. Chen W, Mahadomrongkul V, Berger UV, et al. The glutamate transporter GLT1a is expressed in excitatory axon terminals of mature hippocampal neurons. *J Neurosci*. Feb 4 2004;24(5):1136-48. doi:10.1523/JNEUROSCI.1586-03.2004
8. Melone M, Ciriachi C, Pietrobon D, Conti F. Heterogeneity of Astrocytic and Neuronal GLT-1 at Cortical Excitatory Synapses, as Revealed by its Colocalization With Na+/K+-ATPase alpha Isoforms. *Cereb Cortex*. Jul 22 2019;29(8):3331-3350. doi:10.1093/cercor/bhy203
9. Sharma A, Kazim SF, Larson CS, et al. Divergent roles of astrocytic versus neuronal EAAT2 deficiency on cognition and overlap with aging and Alzheimer's molecular signatures. *Proc Natl Acad Sci U S A*. Oct 22 2019;116(43):21800-21811. doi:10.1073/pnas.1903566116
10. Haroon E, Miller AH, Sanacora G. Inflammation, Glutamate, and Glia: A Trio of Trouble in Mood Disorders. *Neuropsychopharmacology*. Jan 2017;42(1):193-215. doi:10.1038/npp.2016.199
11. Iovino L, Tremblay ME, Civiero L. Glutamate-induced excitotoxicity in Parkinson's disease: The role of glial cells. *J Pharmacol Sci*. Nov 2020;144(3):151-164. doi:10.1016/j.jphs.2020.07.011
12. Rothstein JD, Dykes-Hoberg M, Pardo CA, et al. Knockout of glutamate transporters reveals a major role for astroglial transport in excitotoxicity and clearance of glutamate. *Neuron*. Mar 1996;16(3):675-86. doi:10.1016/s0896-6273(00)80086-0
13. Tanaka K, Watase K, Manabe T, et al. Epilepsy and exacerbation of brain injury in mice lacking the glutamate transporter GLT-1. *Science*. Jun 13 1997;276(5319):1699-702. doi:10.1126/science.276.5319.1699
14. Martinez-Lozada Z, Guillem AM, Robinson MB. Transcriptional Regulation of Glutamate Transporters: From Extracellular Signals to Transcription Factors. *Adv Pharmacol*. 2016;76:103-45. doi:10.1016/bs.apha.2016.01.004
15. Al Awabdh S, Gupta-Agarwal S, Sheehan DF, et al. Neuronal activity mediated regulation of glutamate transporter GLT-1 surface diffusion in rat astrocytes in dissociated and slice cultures. *Glia*. Jul 2016;64(7):1252-64. doi:10.1002/glia.22997
16. Murphy-Royal C, Dupuis JP, Varela JA, et al. Surface diffusion of astrocytic glutamate transporters shapes synaptic transmission. *Nat Neurosci*. Feb 2015;18(2):219-26. doi:10.1038/nn.3901
17. Gonzalez-Gonzalez IM, Garcia-Tardon N, Gimenez C, Zafra F. PKC-dependent endocytosis of the GLT1 glutamate transporter depends on ubiquitylation of lysines located in a C-terminal cluster. *Glia*. Jul 2008;56(9):963-74. doi:10.1002/glia.20670

18. Zhang Y, He X, Meng X, et al. Regulation of glutamate transporter trafficking by Nedd4-2 in a Parkinson's disease model. *Cell Death Dis*. Feb 2 2017;8(2):e2574. doi:10.1038/cddis.2016.454
19. Garcia-Tardon N, Gonzalez-Gonzalez IM, Martinez-Villarreal J, Fernandez-Sanchez E, Gimenez C, Zafra F. Protein kinase C (PKC)-promoted endocytosis of glutamate transporter GLT-1 requires ubiquitin ligase Nedd4-2-dependent ubiquitination but not phosphorylation. *J Biol Chem*. Jun 1 2012;287(23):19177-87. doi:10.1074/jbc.M112.355909
20. Martinez-Villarreal J, Garcia Tardon N, Ibanez I, Gimenez C, Zafra F. Cell surface turnover of the glutamate transporter GLT-1 is mediated by ubiquitination/deubiquitination. *Glia*. Sep 2012;60(9):1356-65. doi:10.1002/glia.22354
21. Vanoni C, Massari S, Losa M, et al. Increased internalisation and degradation of GLT-1 glial glutamate transporter in a cell model for familial amyotrophic lateral sclerosis (ALS). *J Cell Sci*. Oct 15 2004;117(Pt 22):5417-26. doi:10.1242/jcs.01411
22. Susarla BT, Robinson MB. Internalization and degradation of the glutamate transporter GLT-1 in response to phorbol ester. *Neurochem Int*. Mar-Apr 2008;52(4-5):709-22. doi:10.1016/j.neuint.2007.08.020
23. Sha L, Wang X, Li J, et al. Pharmacologic inhibition of Hsp90 to prevent GLT-1 degradation as an effective therapy for epilepsy. *J Exp Med*. Feb 2017;214(2):547-563. doi:10.1084/jem.20160667
24. Voss TD, Gerget M, Linkus B, von Einem B, Landwehrmeyer GB, Lewerenz J. Ubiquitination and the proteasome rather than caspase-3-mediated C-terminal cleavage are involved in the EAAT2 degradation by staurosporine-induced cellular stress. *J Neurochem*. May 2021;157(4):1284-1299. doi:10.1111/jnc.15237
25. Armstrong MJ, Okun MS. Diagnosis and Treatment of Parkinson Disease: A Review. *JAMA*. Feb 11 2020;323(6):548-560. doi:10.1001/jama.2019.22360
26. Hirsch EC, Vyas S, Hunot S. Neuroinflammation in Parkinson's disease. *Parkinsonism Relat Disord*. Jan 2012;18 Suppl 1:S210-2. doi:10.1016/S1353-8020(11)70065-7
27. Sorrentino ZA, Giasson BI, Chakrabarty P. alpha-Synuclein and astrocytes: tracing the pathways from homeostasis to neurodegeneration in Lewy body disease. *Acta Neuropathol*. Jul 2019;138(1):1-21. doi:10.1007/s00401-019-01977-2
28. Spillantini MG, Schmidt ML, Lee VM, Trojanowski JQ, Jakes R, Goedert M. Alpha-synuclein in Lewy bodies. *Nature*. Aug 28 1997;388(6645):839-40. doi:10.1038/42166
29. Deweerdt S. Parkinson's disease: 4 big questions. *Nature*. Oct 27 2016;538(7626):S17. doi:10.1038/538S17a
30. Titova N, Padmakumar C, Lewis SJG, Chaudhuri KR. Parkinson's: a syndrome rather than a disease? *J Neural Transm (Vienna)*. Aug 2017;124(8):907-914. doi:10.1007/s00702-016-1667-6
31. Weingarten CP, Sundman MH, Hickey P, Chen NK. Neuroimaging of Parkinson's disease: Expanding views. *Neurosci Biobehav Rev*. Dec 2015;59:16-52. doi:10.1016/j.neubiorev.2015.09.007
32. Figura M, Kusmierska K, Bucior E, et al. Serum amino acid profile in patients with Parkinson's disease. *PLoS One*. 2018;13(1):e0191670. doi:10.1371/journal.pone.0191670
33. Kim JM, Cha SH, Choi YR, Jou I, Joe EH, Park SM. DJ-1 deficiency impairs glutamate uptake into astrocytes via the regulation of flotillin-1 and caveolin-1 expression. *Sci Rep*. Jun 27 2016;6:28823. doi:10.1038/srep28823
34. O'Gorman Tuura RL, Baumann CR, Baumann-Vogel H. Beyond Dopamine: GABA, Glutamate, and the Axial Symptoms of Parkinson Disease. *Front Neurol*. 2018;9:806. doi:10.3389/fneur.2018.00806
35. Chung EK, Chen LW, Chan YS, Yung KK. Downregulation of glial glutamate transporters after dopamine denervation in the striatum of 6-hydroxydopamine-lesioned rats. *J Comp Neurol*. Dec 1 2008;511(4):421-37. doi:10.1002/cne.21852

36. Chotibut T, Davis RW, Arnold JC, et al. Ceftriaxone increases glutamate uptake and reduces striatal tyrosine hydroxylase loss in 6-OHDA Parkinson's model. *Mol Neurobiol*. Jun 2014;49(3):1282-92. doi:10.1007/s12035-013-8598-0
37. Gu XL, Long CX, Sun L, Xie C, Lin X, Cai H. Astrocytic expression of Parkinson's disease-related A53T alpha-synuclein causes neurodegeneration in mice. *Mol Brain*. Apr 21 2010;3:12. doi:10.1186/1756-6606-3-12
38. Creed RB, Menalled L, Casey B, et al. Basal and Evoked Neurotransmitter Levels in Parkin, DJ-1, PINK1 and LRRK2 Knockout Rat Striatum. *Neuroscience*. Jun 15 2019;409:169-179. doi:10.1016/j.neuroscience.2019.04.033
39. Zhang Y, Meng X, Jiao Z, Liu Y, Zhang X, Qu S. Generation of a Novel Mouse Model of Parkinson's Disease via Targeted Knockdown of Glutamate Transporter GLT-1 in the Substantia Nigra. *ACS Chem Neurosci*. Feb 5 2020;11(3):406-417. doi:10.1021/acschemneuro.9b00609
40. Iwaki H, Blauwendraat C, Leonard HL, et al. Genetic risk of Parkinson disease and progression:: An analysis of 13 longitudinal cohorts. *Neurol Genet*. Aug 2019;5(4):e348. doi:10.1212/NXG.0000000000000348
41. Tolosa E, Vila M, Klein C, Rascol O. LRRK2 in Parkinson disease: challenges of clinical trials. *Nat Rev Neurol*. Feb 2020;16(2):97-107. doi:10.1038/s41582-019-0301-2
42. Longo F, Russo I, Shimshek DR, Greggio E, Morari M. Genetic and pharmacological evidence that G2019S LRRK2 confers a hyperkinetic phenotype, resistant to motor decline associated with aging. *Neurobiol Dis*. Nov 2014;71:62-73. doi:10.1016/j.nbd.2014.07.013
43. Volta M, Beccano-Kelly DA, Paschall SA, et al. Initial elevations in glutamate and dopamine neurotransmission decline with age, as does exploratory behavior, in LRRK2 G2019S knock-in mice. *Elife*. Sep 20 2017;6doi:10.7554/eLife.28377
44. Tozzi A, Tantucci M, Marchi S, et al. Dopamine D2 receptor-mediated neuroprotection in a G2019S Lrrk2 genetic model of Parkinson's disease. *Cell Death Dis*. Feb 12 2018;9(2):204. doi:10.1038/s41419-017-0221-2
45. Longo F, Mercatelli D, Novello S, et al. Age-dependent dopamine transporter dysfunction and Serine129 phospho-alpha-synuclein overload in G2019S LRRK2 mice. *Acta Neuropathol Commun*. Mar 14 2017;5(1):22. doi:10.1186/s40478-017-0426-8
46. Bedford C, Sears C, Perez-Carrion M, Piccoli G, Condliffe SB. LRRK2 Regulates Voltage-Gated Calcium Channel Function. *Front Mol Neurosci*. 2016;9:35. doi:10.3389/fnmol.2016.00035
47. Rivero-Rios P, Romo-Lozano M, Madero-Perez J, et al. The G2019S variant of leucine-rich repeat kinase 2 (LRRK2) alters endolysosomal trafficking by impairing the function of the GTPase RAB8A. *J Biol Chem*. Mar 29 2019;294(13):4738-4758. doi:10.1074/jbc.RA118.005008
48. Gomez-Suaga P, Luzon-Toro B, Churamani D, et al. Leucine-rich repeat kinase 2 regulates autophagy through a calcium-dependent pathway involving NAADP. *Hum Mol Genet*. Feb 1 2012;21(3):511-25. doi:10.1093/hmg/ddr481
49. Bossi E, Fabbrini MS, Ceriotti A. Exogenous protein expression in Xenopus oocytes: basic procedures. *Methods Mol Biol*. 2007;375:107-31. doi:10.1007/978-1-59745-388-2_6
50. Nakamura Y, Kubo H, Kataoka K. Uptake of transmitter amino acids by glial plasmalemmal vesicles from different regions of rat central nervous system. *Neurochem Res*. Sep 1994;19(9):1145-50. doi:10.1007/BF00965148
51. Stigliani S, Zappettini S, Raiteri L, et al. Glia re-sealed particles freshly prepared from adult rat brain are competent for exocytotic release of glutamate. *J Neurochem*. Feb 2006;96(3):656-68. doi:10.1111/j.1471-4159.2005.03631.x
52. Carney KE, Milanese M, van Nierop P, et al. Proteomic analysis of gliosomes from mouse brain: identification and investigation of glial membrane proteins. *J Proteome Res*. Dec 5 2014;13(12):5918-27. doi:10.1021/pr500829z
53. Paluzzi S, Alloisio S, Zappettini S, et al. Adult astroglia is competent for Na+/Ca2+ exchanger-operated exocytotic glutamate release triggered by mild depolarization. *J Neurochem*. Nov 2007;103(3):1196-207. doi:10.1111/j.1471-4159.2007.04826.x

54. Milanese M, Zappettini S, Jacchetti E, et al. In vitro activation of GAT1 transporters expressed in spinal cord gliosomes stimulates glutamate release that is abnormally elevated in the SOD1/G93A(+) mouse model of amyotrophic lateral sclerosis. *J Neurochem*. Apr 2010;113(2):489-501. doi:10.1111/j.1471-4159.2010.06628.x
55. Erichsen MN, Huynh TH, Abrahamsen B, et al. Structure-activity relationship study of first selective inhibitor of excitatory amino acid transporter subtype 1: 2-Amino-4-(4-methoxyphenyl)-7-(naphthalen-1-yl)-5-oxo-5,6,7,8-tetrahydro-4H-chrom ene-3-carbonitrile (UCPH-101). *J Med Chem*. Oct 14 2010;53(19):7180-91. doi:10.1021/jm1009154
56. Shimamoto K, Lebrun B, Yasuda-Kamatani Y, et al. DL-threo-beta-benzyloxyaspartate, a potent blocker of excitatory amino acid transporters. *Mol Pharmacol*. Feb 1998;53(2):195-201. doi:10.1124/mol.53.2.195
57. Battisti I, Ebinezer LB, Lomolino G, Masi A, Arrigoni G. Protein profile of commercial soybean milks analyzed by label-free quantitative proteomics. *Food Chem*. Aug 1 2021;352:129299. doi:10.1016/j.foodchem.2021.129299
58. Cox J, Mann M. MaxQuant enables high peptide identification rates, individualized p.p.b.-range mass accuracies and proteome-wide protein quantification. *Nat Biotechnol*. Dec 2008;26(12):1367-72. doi:10.1038/nbt.1511
59. Streubel-Gallasch L, Giusti V, Sandre M, et al. Parkinson's Disease-Associated LRRK2 Interferes with Astrocyte-Mediated Alpha-Synuclein Clearance. *Mol Neurobiol*. Jul 2021;58(7):3119-3140. doi:10.1007/s12035-021-02327-8
60. Perego C, Vanoni C, Bossi M, et al. The GLT-1 and GLAST glutamate transporters are expressed on morphologically distinct astrocytes and regulated by neuronal activity in primary hippocampal cocultures. *J Neurochem*. Sep 2000;75(3):1076-84. doi:10.1046/j.1471-4159.2000.0751076.x
61. D'Amico A, Soragna A, Di Cairano E, et al. The surface density of the glutamate transporter EAAC1 is controlled by interactions with PDZK1 and AP2 adaptor complexes. *Traffic*. Nov 2010;11(11):1455-70. doi:10.1111/j.1600-0854.2010.01110.x
62. Fan Y, Howden AJM, Sarhan AR, et al. Interrogating Parkinson's disease LRRK2 kinase pathway activity by assessing Rab10 phosphorylation in human neutrophils. *Biochem J*. Jan 2 2018;475(1):23-44. doi:10.1042/BCJ20170803
63. Lis P, Burel S, Steger M, et al. Development of phospho-specific Rab protein antibodies to monitor in vivo activity of the LRRK2 Parkinson's disease kinase. *Biochem J*. Jan 2 2018;475(1):1-22. doi:10.1042/BCJ20170802
64. Zhou J, Sutherland ML. Glutamate transporter cluster formation in astrocytic processes regulates glutamate uptake activity. *J Neurosci*. Jul 14 2004;24(28):6301-6. doi:10.1523/JNEUROSCI.1404-04.2004
65. Gonzalez MI, Susarla BT, Robinson MB. Evidence that protein kinase Calpha interacts with and regulates the glial glutamate transporter GLT-1. *J Neurochem*. Sep 2005;94(5):1180-8. doi:10.1111/j.1471-4159.2005.03330.x
66. Wang Y, Lu S, Qu Z, Wu L, Wang Y. Sonic hedgehog induces GLT-1 degradation via PKC delta to suppress its transporter activities. *Neuroscience*. Dec 4 2017;365:217-225. doi:10.1016/j.neuroscience.2017.09.051
67. Pla A, Pascual M, Guerri C. Autophagy Constitutes a Protective Mechanism against Ethanol Toxicity in Mouse Astrocytes and Neurons. *PLoS One*. 2016;11(4):e0153097. doi:10.1371/journal.pone.0153097
68. Livak KJ, Schmittgen TD. Analysis of relative gene expression data using real-time quantitative PCR and the 2(-Delta Delta C(T)) Method. *Methods*. Dec 2001;25(4):402-8. doi:10.1006/meth.2001.1262
69. Zoltowska KM, Maesako M, Meier J, Berezovska O. Novel interaction between Alzheimer's disease-related protein presenilin 1 and glutamate transporter 1. *Sci Rep*. Jun 7 2018;8(1):8718. doi:10.1038/s41598-018-26888-2

70. Meabon JS, Lee A, Meeker KD, et al. Differential expression of the glutamate transporter GLT-1 in pancreas. *J Histochem Cytochem*. Feb 2012;60(2):139-51. doi:10.1369/0022155411430095
71. Genda EN, Jackson JG, Sheldon AL, et al. Co-compartmentalization of the astroglial glutamate transporter, GLT-1, with glycolytic enzymes and mitochondria. *J Neurosci*. Dec 14 2011;31(50):18275-88. doi:10.1523/JNEUROSCI.3305-11.2011
72. Tian G, Lai L, Guo H, et al. Translational control of glial glutamate transporter EAAT2 expression. *J Biol Chem*. Jan 19 2007;282(3):1727-37. doi:10.1074/jbc.M609822200
73. Gendreau S, Voswinkel S, Torres-Salazar D, et al. A trimeric quaternary structure is conserved in bacterial and human glutamate transporters. *J Biol Chem*. Sep 17 2004;279(38):39505-12. doi:10.1074/jbc.M408038200
74. Swanson RA, Liu J, Miller JW, et al. Neuronal regulation of glutamate transporter subtype expression in astrocytes. *J Neurosci*. Feb 1 1997;17(3):932-40.
75. Schlag BD, Vondrasek JR, Munir M, et al. Regulation of the glial Na+-dependent glutamate transporters by cyclic AMP analogs and neurons. *Mol Pharmacol*. Mar 1998;53(3):355-69. doi:10.1124/mol.53.3.355
76. Raiteri L, Zappettini S, Milanese M, Fedele E, Raiteri M, Bonanno G. Mechanisms of glutamate release elicited in rat cerebrocortical nerve endings by 'pathologically' elevated extraterminal K+ concentrations. *J Neurochem*. Nov 2007;103(3):952-61. doi:10.1111/j.1471-4159.2007.04784.x
77. Weber W. Ion currents of Xenopus laevis oocytes: state of the art. *Biochim Biophys Acta*. Oct 15 1999;1421(2):213-33. doi:10.1016/s0005-2736(99)00135-2
78. Klumperman J, Raposo G. The complex ultrastructure of the endolysosomal system. *Cold Spring Harb Perspect Biol*. May 22 2014;6(10):a016857. doi:10.1101/cshperspect.a016857
79. Fermie J, Liv N, Ten Brink C, et al. Single organelle dynamics linked to 3D structure by correlative live-cell imaging and 3D electron microscopy. *Traffic*. May 2018;19(5):354-369. doi:10.1111/tra.12557
80. Groger A, Kolb R, Schafer R, Klose U. Dopamine reduction in the substantia nigra of Parkinson's disease patients confirmed by in vivo magnetic resonance spectroscopic imaging. *PLoS One*. 2014;9(1):e84081. doi:10.1371/journal.pone.0084081
81. Iwasaki Y, Ikeda K, Shiojima T, Kinoshita M. Increased plasma concentrations of aspartate, glutamate and glycine in Parkinson's disease. *Neurosci Lett*. Oct 12 1992;145(2):175-7. doi:10.1016/0304-3940(92)90015-y
82. Morales I, Sanchez A, Rodriguez-Sabate C, Rodriguez M. The astrocytic response to the dopaminergic denervation of the striatum. *J Neurochem*. Oct 2016;139(1):81-95. doi:10.1111/jnc.13684
83. Zhu YF, Wang WP, Zheng XF, et al. Characteristic response of striatal astrocytes to dopamine depletion. *Neural Regen Res*. Apr 2020;15(4):724-730. doi:10.4103/1673-5374.266917
84. Tong J, Ang LC, Williams B, et al. Low levels of astroglial markers in Parkinson's disease: relationship to alpha-synuclein accumulation. *Neurobiol Dis*. Oct 2015;82:243-253. doi:10.1016/j.nbd.2015.06.010
85. McGeer PL, McGeer EG. Glial reactions in Parkinson's disease. *Mov Disord*. Mar 15 2008;23(4):474-83. doi:10.1002/mds.21751
86. Flores-Cuadrado A, Saiz-Sanchez D, Mohedano-Moriano A, et al. Astrogliosis and sexually dimorphic neurodegeneration and microgliosis in the olfactory bulb in Parkinson's disease. *NPJ Parkinsons Dis*. Jan 21 2021;7(1):11. doi:10.1038/s41531-020-00154-7
87. Ramos-Gonzalez P, Mato S, Chara JC, Verkhratsky A, Matute C, Cavaliere F. Astrocytic atrophy as a pathological feature of Parkinson's disease with LRRK2 mutation. *NPJ Parkinsons Dis*. Mar 30 2021;7(1):31. doi:10.1038/s41531-021-00175-w

88. Xiong Y, Neifert S, Karuppagounder SS, et al. Robust kinase- and age-dependent dopaminergic and norepinephrine neurodegeneration in LRRK2 G2019S transgenic mice. *Proc Natl Acad Sci U S A*. Feb 13 2018;115(7):1635-1640. doi:10.1073/pnas.1712648115
89. Iannotta L, Biosa A, Kluss JH, et al. Divergent Effects of G2019S and R1441C LRRK2 Mutations on LRRK2 and Rab10 Phosphorylations in Mouse Tissues. *Cells*. Oct 22 2020;9(11)doi:10.3390/cells9112344
90. Miklossy J, Arai T, Guo JP, et al. LRRK2 expression in normal and pathologic human brain and in human cell lines. *J Neuropathol Exp Neurol*. Oct 2006;65(10):953-63. doi:10.1097/01.jnen.0000235121.98052.54
91. Booth HDE, Hirst WD, Wade-Martins R. The Role of Astrocyte Dysfunction in Parkinson's Disease Pathogenesis. *Trends Neurosci*. Jun 2017;40(6):358-370. doi:10.1016/j.tins.2017.04.001
92. Kam TI, Hinkle JT, Dawson TM, Dawson VL. Microglia and astrocyte dysfunction in parkinson's disease. *Neurobiol Dis*. Oct 2020;144:105028. doi:10.1016/j.nbd.2020.105028
93. Rose EM, Koo JC, Antflick JE, Ahmed SM, Angers S, Hampson DR. Glutamate transporter coupling to Na,K-ATPase. *J Neurosci*. Jun 24 2009;29(25):8143-55. doi:10.1523/JNEUROSCI.1081-09.2009
94. Funk N, Munz M, Ott T, et al. The Parkinson's disease-linked Leucine-rich repeat kinase 2 (LRRK2) is required for insulin-stimulated translocation of GLUT4. *Sci Rep*. Mar 14 2019;9(1):4515. doi:10.1038/s41598-019-40808-y
95. Morel E, Parton RG, Gruenberg J. Annexin A2-dependent polymerization of actin mediates endosome biogenesis. *Dev Cell*. Mar 2009;16(3):445-57. doi:10.1016/j.devcel.2009.01.007
96. Delevoye C, Heiligenstein X, Ripoll L, et al. BLOC-1 Brings Together the Actin and Microtubule Cytoskeletons to Generate Recycling Endosomes. *Curr Biol*. Jan 11 2016;26(1):1-13. doi:10.1016/j.cub.2015.11.020

Figure 1

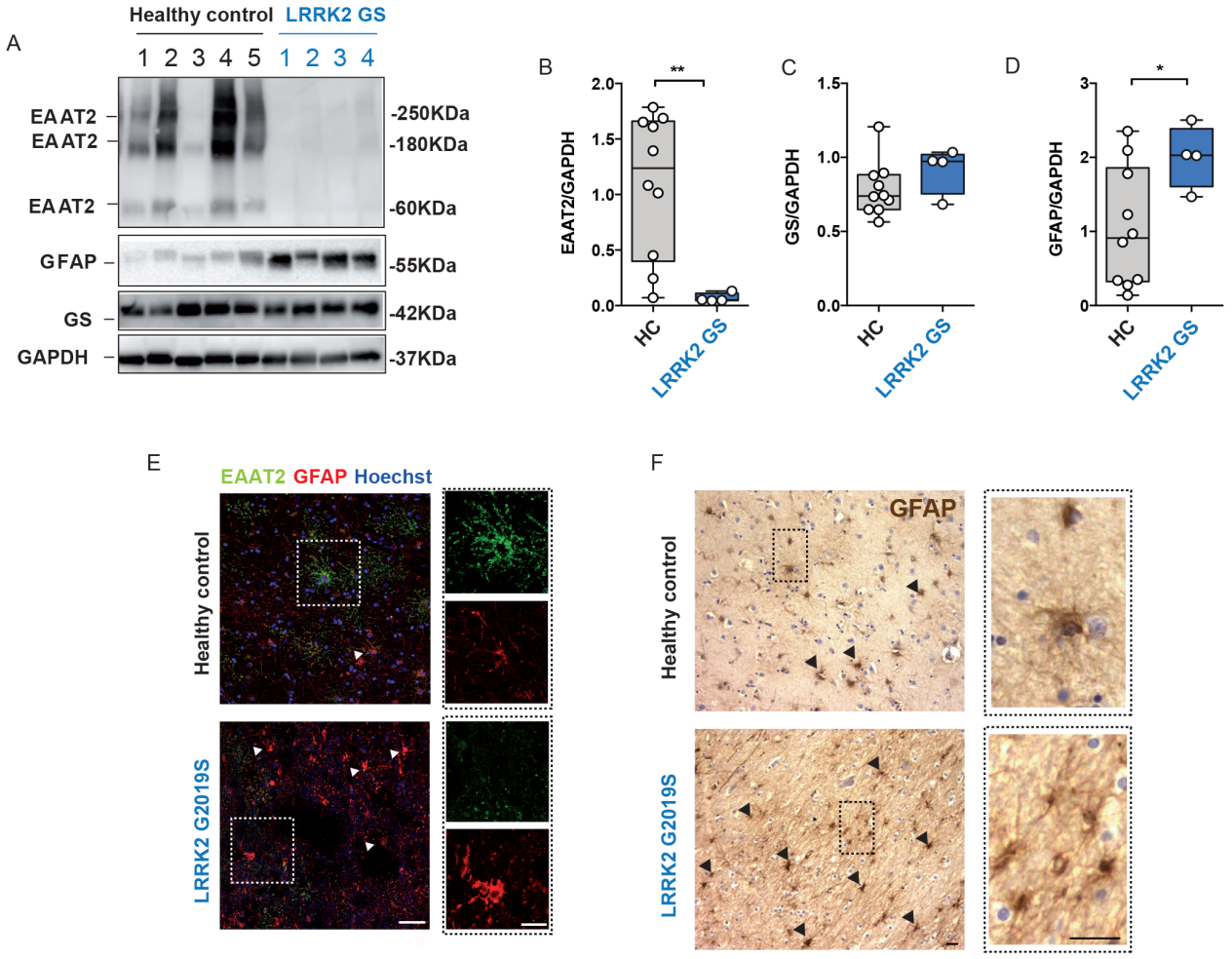

Figure 1 EAAT2 levels are decreased in human LRRK2 G2019S brains
A) Western blot analysis of human LRRK2 G2019S basal ganglia lysates and healthy controls using anti-EAAT2, anti-GFAP, anti-GS; B-D) Relative quantification of band intensity was performed using ImageJ and normalized to the housekeeping protein GAPDH (n=10 age-matched control samples and n=4 LRRK2 G2019S basal ganglia samples); E) Representative double-labeling images for EAAT2 (green) and GFAP (red) in LRRK2 G2019S human basal ganglia and age-matched control; scale bar 50 µm, insets 20 µm; f) Representative images of DAB-immunostaining for GFAP in LRRK2 G2019S human striatum and age-matched control; scale bar 25 µm, insets 10 µm; arrowheads in E) and F) indicate the presence of GFAP positive cells. Statistical analysis in b was performed using Mann-Whitney test and in c-d using Unpaired T-test.

Figure 2

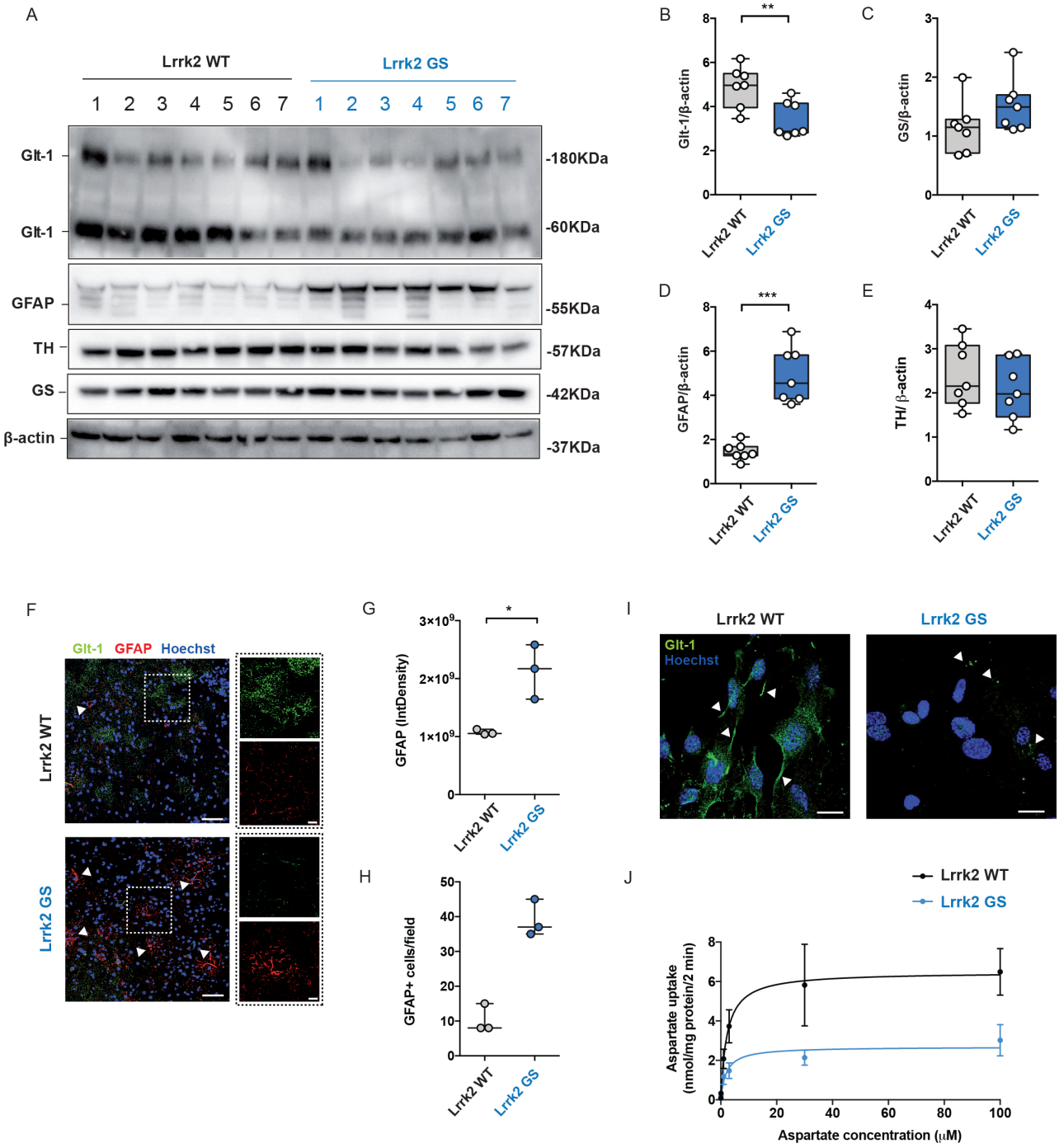

Figure 2 Glutamate transporter is downregulated in the striatum of Lrrk2 G2019S mice
A) Western blot analysis of Lrrk2 WT and Lrrk2 G2019S striatal lysates using anti-Glt-1, anti-GFAP, anti-TH antibodies and anti-GS; B-E) Relative quantification of band intensity was performed using ImageJ and normalized to β-actin (n=7 striatal samples for both Lrrk2 WT and G2019S 4-months old mice); F) Representative confocal double-labeling images for Glt-1 (green) and GFAP (red) in Lrrk2 WT and G2019S striatal slices; scale bar 50 µm, insets 20 µm; G-H) Quantification of GFAP IntDen and GFAP^{+} cells in the dorsal striatum of Lrrk2 WT and G2019S mice, three different fields per animal were collected, n=3 animals for each genotype; I)

Representative confocal images of the cellular distribution (arrowheads) of the endogenous Glt-1 in primary striatal astrocytes derived from Lrrk2 WT and Lrrk2 G2019S mice treated with dbcAMP (500 μM) for ten days; bar 20 μm; J) Striatal gliosomes from Lrrk2 WT and Lrrk2 G2019S 4-month old mice were exposed for 2 min at 37 °C to increasing concentration of [^{3}H]D-Asp (0.03, 0.1, 1, 3, 30 and 100 μM) in the presence of 10 μM UCPH to exclude [^{3}H]D-Asp uptake by Glast. The specific [^{3}H]D-Asp uptake is expressed as nmol/mg protein/2 min; the kinetic parameters V_{max} and K_m were obtained by fitting data with the Michaelis-Menten equation (n=4 independent experiments for each group). Statistical analysis in B-E and J was performed using Unpaired T-test; statistical analysis in G-H was performed using Mann-Whitney test.

Figure 3

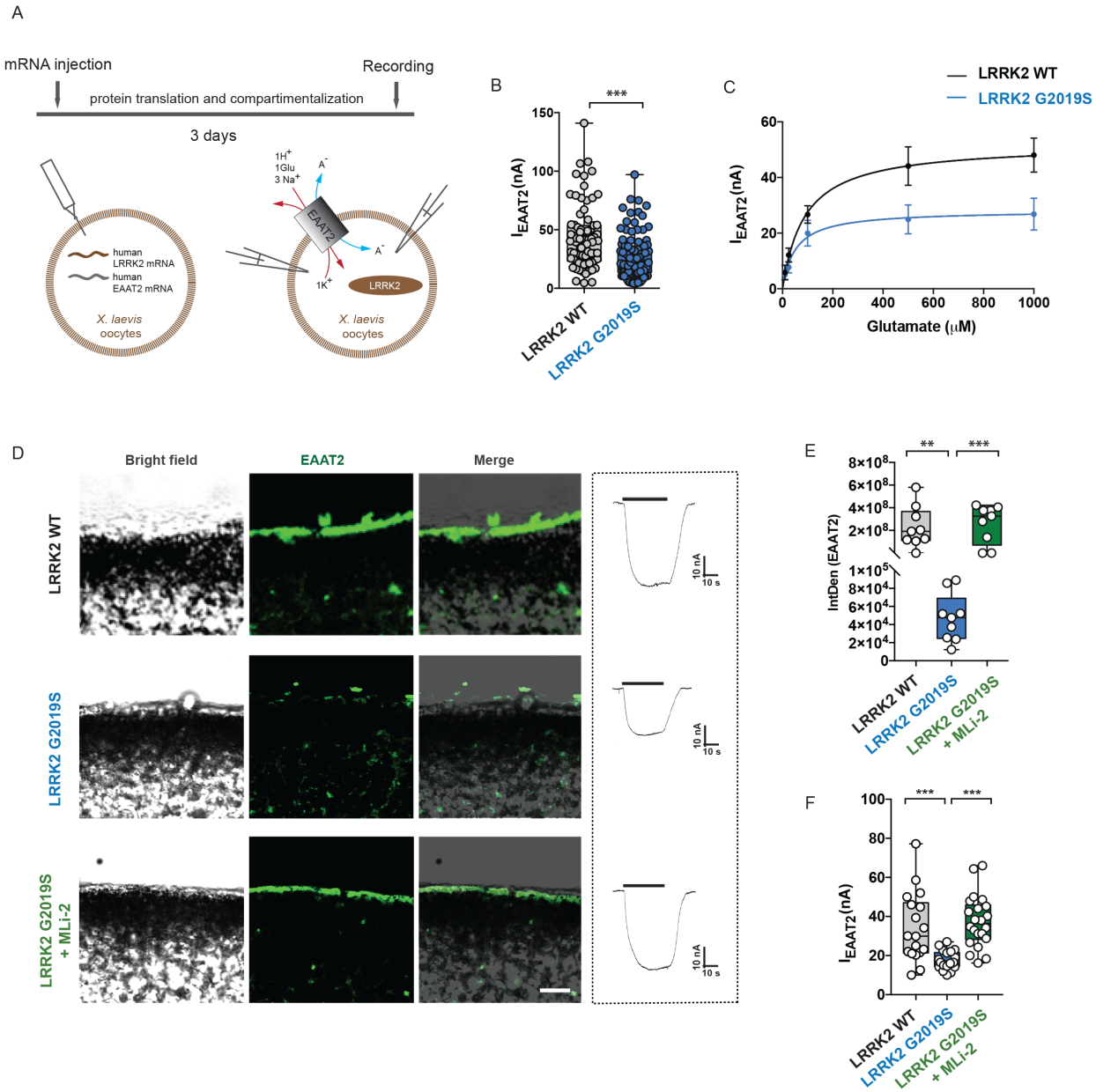

Figure 3 LRRK2 G2019S alters EAAT2 electrophysiological properties
A) Schematic outline of the experimental setup. Oocytes were co-injected with mRNA of EAAT2 and human LRRK2 (WT or G2019S) and glutamate transport associated-currents were recorded using the two-electrode voltage-clamp technique; B) The bar graph represents current amplitudes elicited in oocytes co-expressing EAAT2 and LRRK2 WT (n=79, 12 frogs) or G2019S (n=122, 12 frogs). Glutamate application was at 1 mM and the holding potential at −60 mV; C) Transport-associated currents in oocytes co-expressing EAAT2 and LRRK2 WT or G2019S as a function of glutamate concentration. The kinetic parameters I_{max} and aK_m were obtained by fitting data with the Michaelis-Menten equation (n=6; 2 frogs); D) Representative bright field (left column) or fluorescence (middle column, merge on the right column) images of oocyte slices co-expressing EAAT2 (green) and LRRK2 WT or G2019S, with or without 90 min MLi-2 (200 nM) treatment, scale bar 20 μm. Representative traces of the recorded transport current in all the three groups are

shown on the right; E) Quantitative analysis of the IntDen of the EAAT2 signal at the oocyte membrane was performed in three different fields for each oocyte, n=3 independent oocytes for each group; F) The bar graph represents current amplitudes elicited in oocytes co-expressing EAAT2 and LRRK2 WT (n=18, 6 frogs), G2019S (n=22, 6 frogs) or G2019S+MLi-2 (n=22, 6 frogs). Statistical analysis in B was performed using Mann-Whitney test, in E using Kruskal-Wallis test followed by Dunn's multiple comparisons test. Statistical analysis in F was performed using Unpaired T-test to compare EAAT2+LRRK2 WT to EAAT2+G2019S injected oocytes and with Paired T-test to compare EAAT2+G2019S oocytes before and after LRRK2 inhibition.

Figure 4

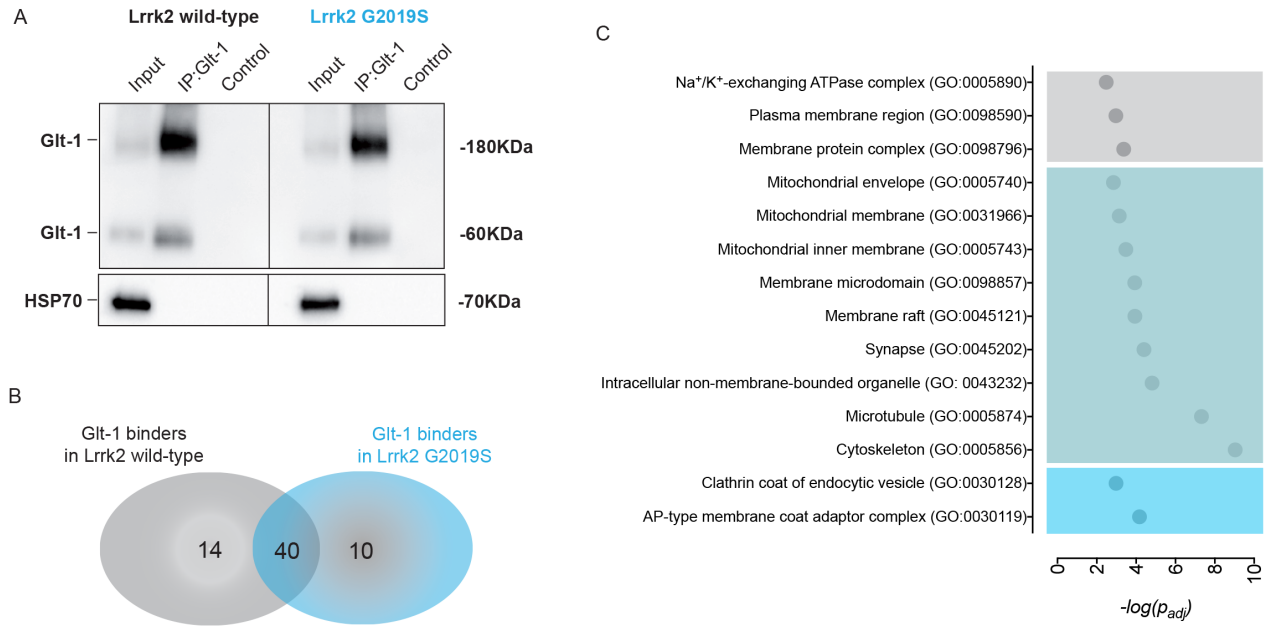

Figure 4 Screening of Glt-1 protein-protein interactions
A) Striatal Glt-1 immunoprecipitated from Lrrk2 WT and G2019S brains was resolved by immunoblotting. Anti-HSP70 was applied to normalize for protein content; B) Venn diagram summary of interacting proteins, colored for different background (grey for Lrrk2 WT, light blue for Lrrk2 G2019S, dark blue for Lrrk2 WT and G2019S shared interacting proteins); C) Selected GO term enrichments from CC categories using gProfiler were plotted using -log(P*adj*) values.

Figure 5

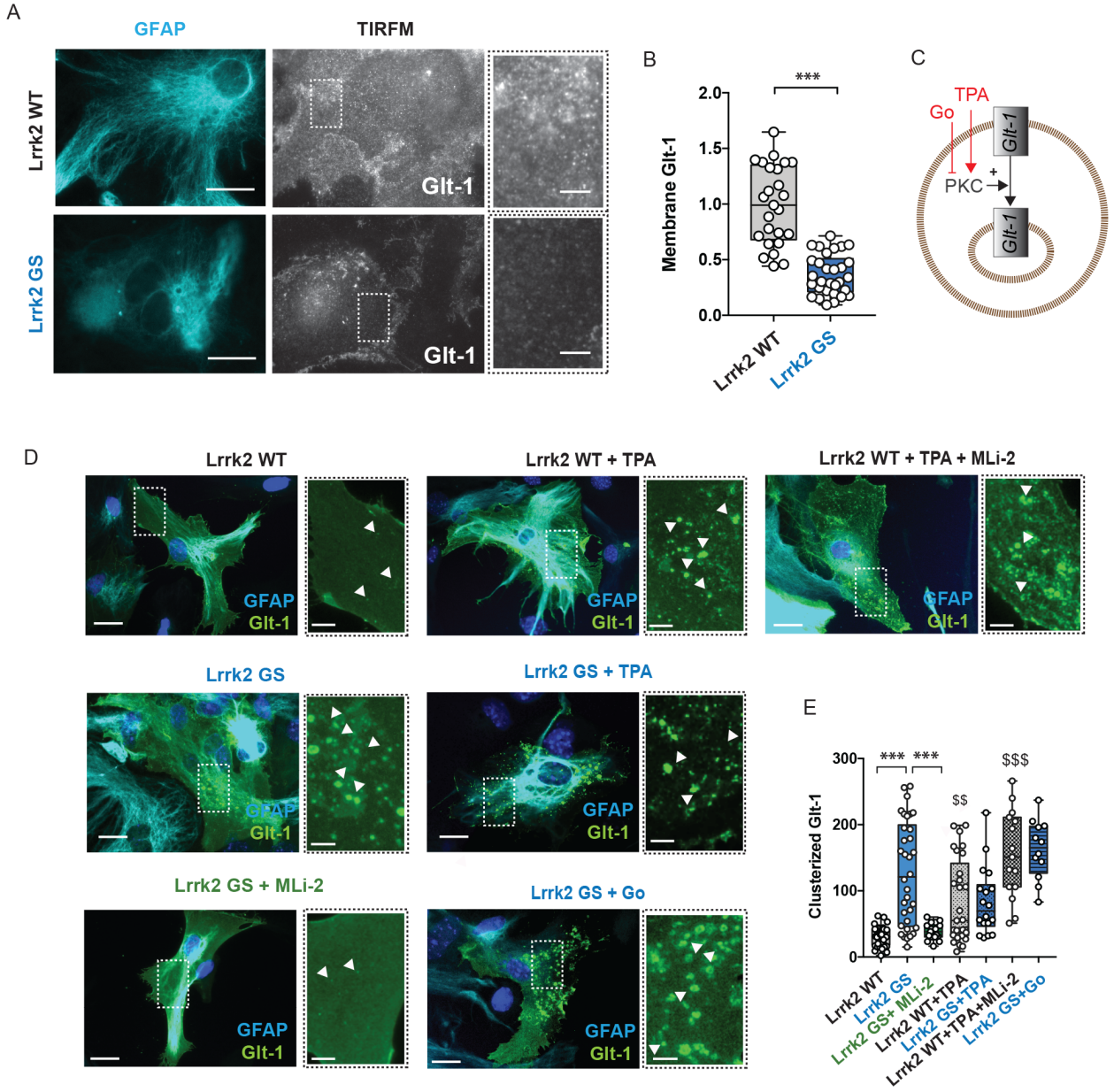

Figure 5 Astroglial Glt-1 is mislocalized in the presence of Lrrk2 G2019S mutation
A) Representative TIRFM images of Glt-1 localization in Lrrk2 WT and Lrrk2 G2019S astrocytes transfected with GFP-Glt1 (gray) and stained with GFAP (cyan). Scale bar 20 µm; B) Quantification of the GFP-Glt-1 mean fluorescence performed in TIRFM images (n = 25 cells from n=2 independent astrocyte cultures derived from Lrrk2 WT and G2019S were considered for the analysis); C) Schematic representation of TPA and Go 6976 effects on PKC activity; D) Representative epifluorescence images of Glt-1 intracellular clusters in Lrrk2 WT and Lrrk2 G2019S astrocytes transfected with Flag-Glt-1 (green) and stained with GFAP (cyan) under basal condition and after pharmacological treatment; Scale bar 20 µm, insets 5 µm; E) Quantification of the number of Glt-1-positive clusters per cell under basal condition and after pharmacological treatment using Lrrk2 inhibitor MLi-2 (90 min), the PKC activator TPA (20 min), the co-

application of TPA and Mli-2 and the application of the PKC inhibitor Go 6976 (Go; 90 min). Number of independent cell cultures used: Lrrk2 WT (n = 6), Lrrk2 G2019S (n = 6), Lrrk2 G2019S+MLi-2 (n = 4), Lrrk2 WT+TPA (n=3), Lrrk2 WT+TPA+MLI-2 (n=3) Lrrk2 G2019S+TPA (n=3) and Lrrk2 G2019S+Go 6976 (n=3). Three cells analyzed for each independent cell cultures. Statistical analysis in B was performed using One-way ANOVA test followed by Tukey's multiple comparisons test. Statistical analysis in E was performed using Kruskal-Wallis test followed by Dunn's multiple comparisons test ($ vs Lrrk2 WT).

Figure 6

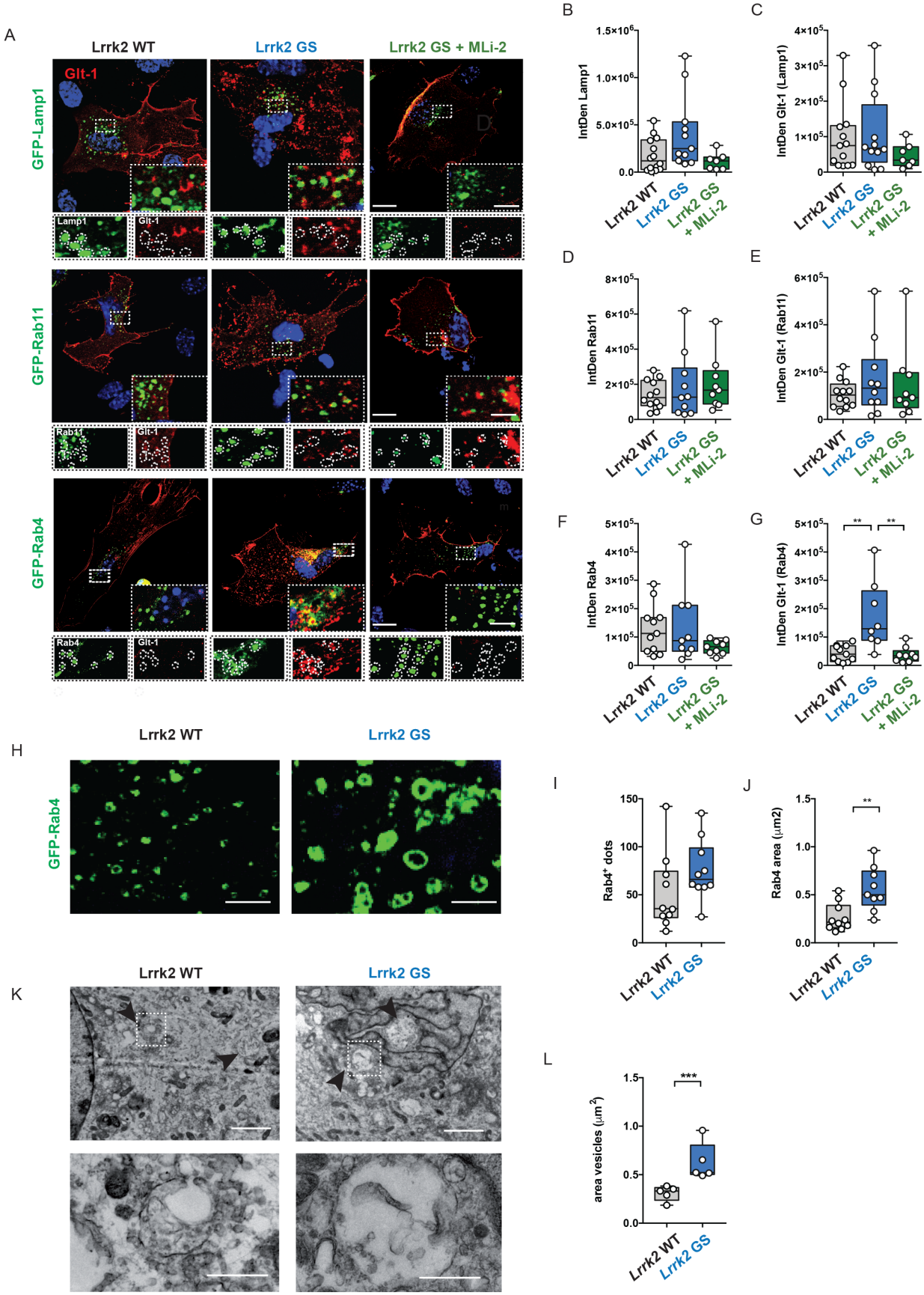

Figure 6 Lrrk2 G2019S enhances Glt-1 accumulation in Rab4-positive organelles

A) Representative z-stack confocal images of primary astrocytes from Lrrk2 WT and Lrrk2 G2019S mice transfected with Flag-Glt-1 and GFP-Lamp1, GFP-Rab11 or GFP-Rab4 under basal conditions or upon treatment with MLi-2 inhibitor. Insets show Lamp1-, Rab11- or Rab4-positive area and the localization of Glt-1 in the indicated ROIs. Scale bars: 20 µm; insets 5 µm; B-C) Quantitative analysis of Lamp1 IntDen and Glt-1 IntDen in Lamp1 compartment; D-E) Quantitative analysis of Rab11 IntDen and Glt-1 IntDen in Rab11 compartment; F-G) Quantitative analysis of Rab4 IntDen and Glt-1 IntDen in Rab4 compartment; Number of independent cell cultures used Lrrk2 WT (n = 4), Lrrk2 G2019S (n = 4) and Lrrk2 G2019S +MLi-2 (n = 3). H) Representative confocal microscopy images of Lrrk2 WT and G2019S primary striatal astrocytes transfected with GFP-Rab4 and Flag-Glt-1. Scale bars: 2 µm; I-J) Quantification of Rab4-positive vesicle number and area. Number of independent cell cultures used Lrrk2 WT (n = 4), Lrrk2 G2019S (n = 4); K) Representative TEM images of Lrrk2 WT and G2019S endosomal-like structures in primary striatal astrocytes transfected with GFP-Rab4 and Flag-Glt-1 (top: scale bars: 5 µm; bottom: scale bars: 500 nm); L) Quantification of the area of endosomal-like structures (n=5 independent astrocytes analyzed for each group, ten independent fields were analyzed for quantification). Statistical analysis in B-G was performed using One-way ANOVA test followed by Tukey's multiple comparison test. Statistical analysis in I-J-L was performed using Unpaired t-tests; Mann-Whitney test.

Figure 7

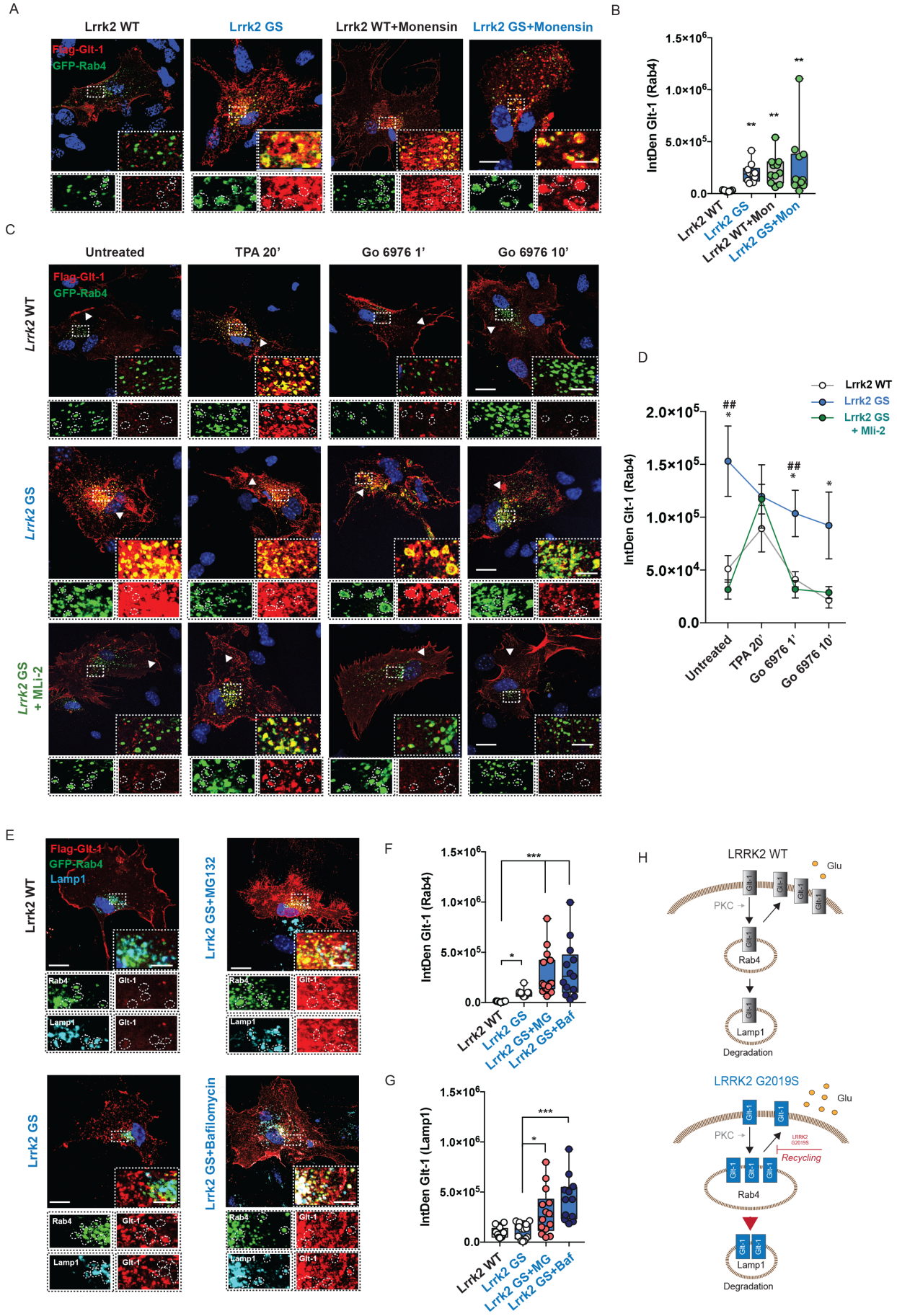
A
Lrrk2 WT
Lrrk2 GS
Lrrk2 WT+Monensin
Lrrk2 GS+Monensin
Flag-Glt-1
GFP-Rab4
B
IntDen Glt-1 (Rab4)
1.5×10^6
1.0×10^6
5.0×10^5
0.0
Lrrk2 WT
Lrrk2 GS
Lrrk2 WT+Mon
Lrrk2 GS+Mon
C
Untreated
TPA 20'
Go 6976 1'
Go 6976 10'
Lrrk2 WT
Lrrk2 GS
Lrrk2 GS + MLi-2
D
Lrrk2 WT
Lrrk2 GS
Lrrk2 GS + Mli-2
IntDen Glt-1 (Rab4)
2.0×10^5
1.5×10^5
1.0×10^5
5.0×10^4
0.0
Untreated
TPA 20'
Go 6976 1'
Go 6976 10'
E
Lrrk2 WT
Lrrk2 GS+MG132
Lrrk2 GS
Lrrk2 GS+Bafilomycin
Flag-Glt-1
GFP-Rab4
Lamp1
Rab4
Glt-1
F
IntDen Glt-1 (Rab4)
Lrrk2 WT
Lrrk2 GS
Lrrk2 GS+MG
Lrrk2 GS+Baf
G
IntDen Glt-1 (Lamp1)
Lrrk2 WT
Lrrk2 GS
Lrrk2 GS+MG
Lrrk2 GS+Baf
H
LRRK2 WT
Glu
PKC
Rab4
Lamp1
Degradation
LRRK2 G2019S
Glu
PKC
Recycling
Rab4
Lamp1
Degradation

Figure 7 G2019S pathogenic Lrrk2 mutation impacts on Glt-1 recycling and turnover
A) Representative confocal images of primary striatal Lrrk2 WT and G2019S astrocytes under basal conditions and treated with the recycling blocker Monensin (35 µM, 40 min). Insets show the Rab4-positive area and the localization of Glt-1 in the indicated ROIs. Scale bars: 20 µm; insets 5 µm; B) Quantitative analysis of Glt-1 IntDen in Rab4-positive compartment; number of independent cell cultures used Lrrk2 WT (n = 2), Lrrk2 WT+Monensin (n = 2), Lrrk2 G2019S (n = 2) and Lrrk2 G2019S +Monensin (n = 2); C) Representative z-stack confocal images of primary Lrrk2 WT and G2019S (with or without MLi-2) striatal astrocytes transfected with Flag-Glt-1 (red) and GFP-Rab4 (green). The insets show Rab4-positive area and the localization of Glt-1 in these ROIs; scale bar 20 µm; insets 5 µm; D) Quantification of Glt-1 IntDen in Rab4 compartment in the four selected experimental time points. n=2 independent astrocyte cultures were considered for the analysis; E) Representative z-stack confocal images of primary striatal Lrrk2 WT and G2019S astrocytes transfected with GFP-Rab4 and Flag-Glt-1 (red) and labeled for endogenous Lamp1 (far red, pseudocolored in blue). Insets show Rab4 and Lamp1-positve area and the localization of Glt-1 in these ROIs. Scale bar 20 µm; insets 5 µm; F) Quantification of Glt-1 IntDen in the Rab4-positive vesicles under basal conditions or upon MG132 or Bafilomycin application; n=2 independent astrocyte cultures were considered for the analysis. G) Quantification of Glt-1 IntDen in the endogenous Lamp1-positive structures under basal conditions or upon MG132 or Bafilomycin application; n=2 independent astrocyte cultures were considered for the analysis. H) Schematic representation of Glt-1 trafficking in Lrrk2 WT and Lrrk2 G2019S astrocytes. Statistical analysis in B,F-G was performed using Kruskal-Wallis test followed by Dunn's multiple comparisons test. Statistical analysis in D was performed using One-way ANOVA test followed by Tukey's multiple comparisons test (* Lrrk2 WT vs Lrrk2 G2019S, ## Lrrk2 G2019S vs Lrrk2 G2019S+MLi-2).

Supplementary Figures

Supplementary Figure 1

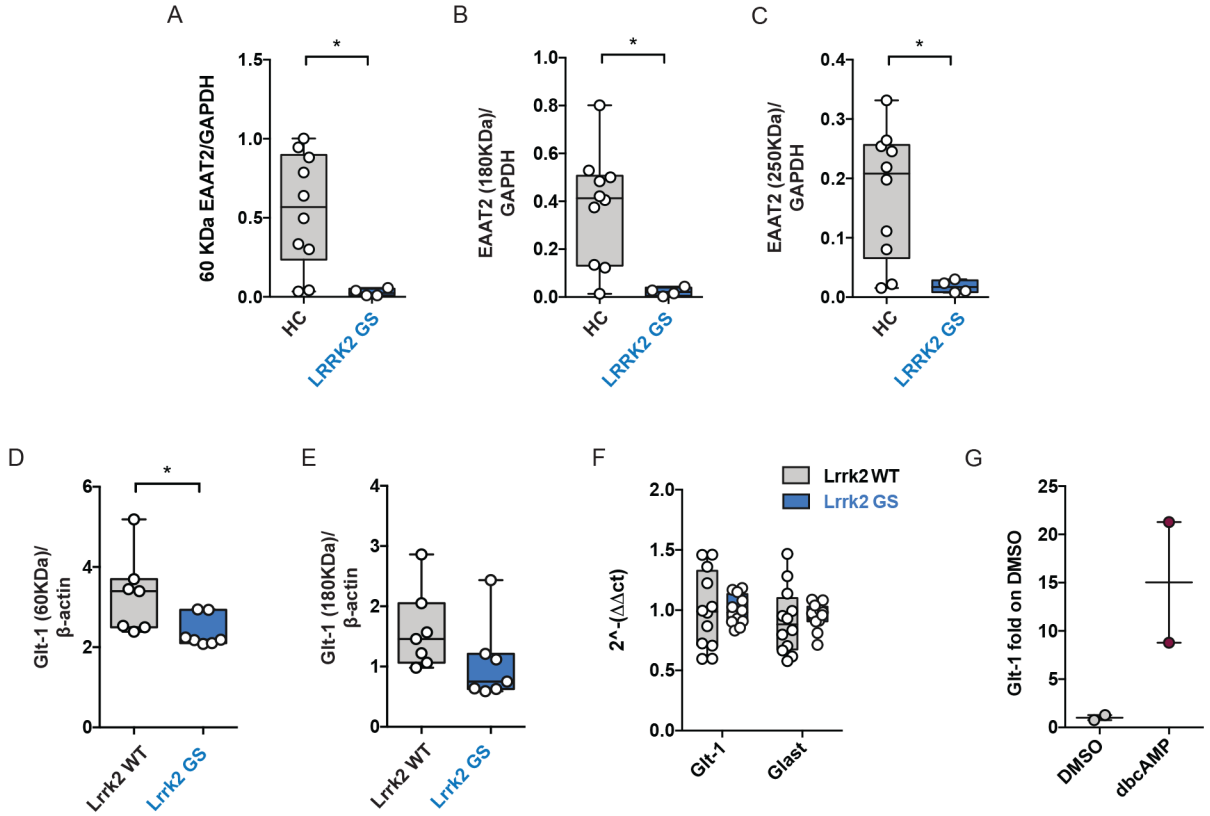

Supplementary Figure 1
A-C) Western blot quantification of the monomeric fractions (60 KDa) as well as of the multimeric fractions (180 KDa and 250 KDa) of EAAT2 in LRRK2 G2019S PD patients (n=4) compared to healthy controls (n=10); D-E) Quantification of the 60 KDa and 180 KDa Glt-1 bands in Lrrk2 G2019S and Lrrk2 WT mice; n=7 animals for each genotype; F) qPCR analysis of Glt-1 and Glast mRNA in the striatum of Lrrk2 WT and Lrrk2 G2019S mice; n=12 animals for each genotype; G) qPCR analysis of Glt-1 mRNA in primary Lrrk2 WT striatal astrocytes treated with or without dbcAMP for 10 days; n=2 independent cell cultures. Statistical analysis was performed in A-C and F using Unpaired T-test and in D-E using Mann-Whitney test.

Supplementary Figure 2

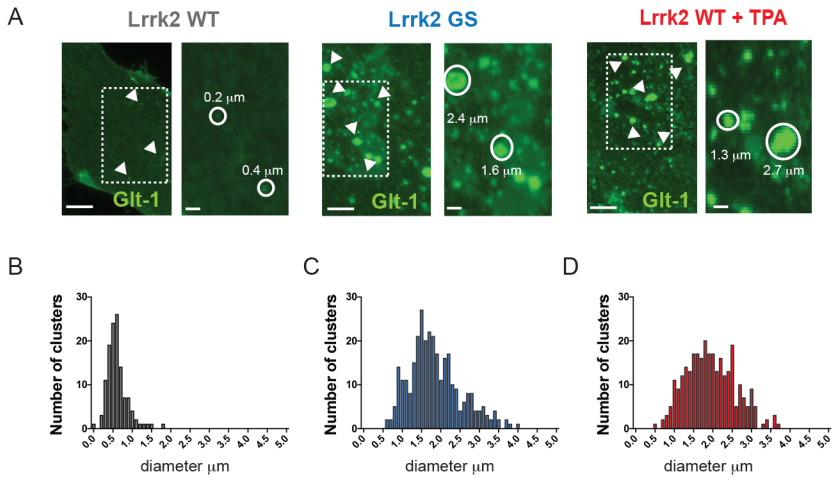

Supplementary Figure 2

A) Representative epifluorescence images of Glt-1 clusters in Flag-Glt-1 transfected primary striatal astrocytes from Lrrk2 WT (untreated or treated with TPA) and from Lrrk2 G2019S astrocytes. Scale bars 5 µm; insets 1 µm. B) Frequency distribution of Glt-1 cluster diameter in untreated Lrrk2 WT (grey bars); C) Frequency distribution of Glt-1 cluster diameter in Lrrk2 G2019S (blue bars); D) Frequency distribution of Glt-1 cluster diameter in Lrrk2 WT treated with TPA (d; red bars); n=5 independent astrocytes analyzed for each group.

Supplementary Figure 3

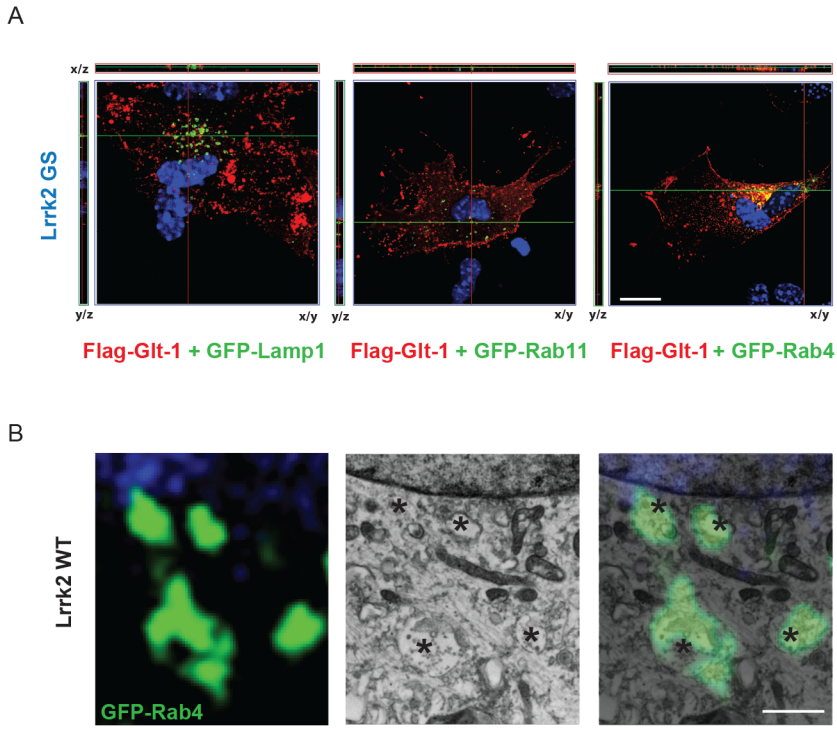

Supplementary Figure 3
A) Orthogonal z-stack projections of Lrrk2 G2019S astrocytes co-transfected with Flag-Glt-1 (red) and Lamp1-GFP, Rab11-GFP or Rab4-GFP (green). Scale bar 20 µm. B**)** Representative confocal (left panel), electron microscopy (middle panel) and merge (right panel) image of a Lrrk2 WT primary astrocyte transfected with Rab4-GFP (green). The image reveals the co-localization of early endosomal structures identified by transmission microscopy with the GFP-Rab4-positive vesicles identified by confocal microscopy; scale bar: 1 µm